



**University of
Zurich** UZH

**Zurich Open Repository and
Archive**

University of Zurich
University Library
Strickhofstrasse 39
CH-8057 Zurich
www.zora.uzh.ch

Year: 2023

Meteoric ^{10}Be as a tracer of soil redistribution rates and reconstruction tool of loess-mantled soils (SW, Poland)

Beata Kowalska, Joanna ; Egli, Markus ; Vögtli, Martina ; Tikhomirov, Dmitry ; Łabaz, Beata ; Christl, Marcus ; Waroszewski, Jarosław

DOI: <https://doi.org/10.1016/j.geoderma.2023.116451>

Posted at the Zurich Open Repository and Archive, University of Zurich

ZORA URL: <https://doi.org/10.5167/uzh-252023>

Journal Article

Published Version



The following work is licensed under a Creative Commons: Attribution 4.0 International (CC BY 4.0) License.

Originally published at:

Beata Kowalska, Joanna; Egli, Markus; Vögtli, Martina; Tikhomirov, Dmitry; Łabaz, Beata; Christl, Marcus; Waroszewski, Jarosław (2023). Meteoric ^{10}Be as a tracer of soil redistribution rates and reconstruction tool of loess-mantled soils (SW, Poland). *Geoderma*, 433:116451.

DOI: <https://doi.org/10.1016/j.geoderma.2023.116451>

Meteoric ^{10}Be as a tracer of soil redistribution rates and reconstruction tool of loess-mantled soils (SW, Poland)

Journal Article

Author(s):

Kowalska, Joanna Beata; Egli, Markus; Vöggtli, Martina; Tikhomirov, Dmitry; Łabaz, Beata; [Christl, Marcus](#) ; Waroszewski, Jarosław

Publication date:

2023-05

Permanent link:

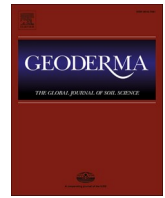
<https://doi.org/10.3929/ethz-b-000607288>

Rights / license:

[Creative Commons Attribution 4.0 International](#)

Originally published in:

Geoderma 433, <https://doi.org/10.1016/j.geoderma.2023.116451>



Meteoric ^{10}Be as a tracer of soil redistribution rates and reconstruction tool of loess-mantled soils (SW, Poland)

Joanna Beata Kowalska^a, Markus Egli^b, Martina Vögtli^b, Dmitry Tikhomirov^b, Beata Łabaz^a, Marcus Christl^c, Jarosław Waroszewski^{a,*}

^a Institute of Soil Science, Plant Nutrition and Environmental Protection, Wrocław University of Environmental and Life Sciences, Wrocław, Poland

^b Department of Geography, University of Zürich, Zürich, Switzerland

^c Laboratory of Ion Beam Physics, ETH-Zurich, 8093 Zurich, Switzerland

ARTICLE INFO

Handling Editor: Morgan Cristine L.S.

Keywords:

Long-term erosion rates
Loess mantles
Cosmogenic nuclides
Polygenesis

ABSTRACT

Loess deposits are terrestrial archives that record progressive deposition and erosion events of varying intensities. Data on long-term erosion rates are crucial for tracking changes in the stability of a loess mantle and reconstructing the evolution of loess-enriched soils. We used meteoric ^{10}Be to i) define the factors responsible for its distribution along the profile, ii) determine long-term erosion rates in loess-enriched polygenetic soils characterised by illuviation processes, and iii) evaluate initial soil thickness and stability over time. Distribution of meteoric ^{10}Be along the soil profiles was mainly driven by its translocation with clay particles and accumulation in the illuvial horizons. However, in some cases (loess over serpentinite), the highest meteoric ^{10}Be content was measured in the C horizons which may be related to the longer exposure of serpentinite to meteoric ^{10}Be deposition before the occurrence of a major loess accumulation event. The estimated long-term erosion rates greatly depend on the assumed environmental settings and were in the range of about $0.1\text{--}3\text{ t ha}^{-1}\text{ yr}^{-1}$. Based on the soil redistribution rates, we reconstructed the removed loess layer which was from a few dm to about 3 m. The results indicate four main soil evolutionary phases: a) pre-exposure of sediments to meteoric ^{10}Be accumulation; b) formation of thick loess mantles during the Last Glacial Maximum; c) erosion events between 21 and 11.6 ka that significantly shallowed the initial loess mantles; d) pedogenesis (with subsoil clay accumulation) in the Holocene within the thinner relicts of the former Late Pleistocene loess mantle followed by a recent and strong erosional phase due to human impact. These phases are also believed to have occurred in several other areas of Central Europe.

1. Introduction

Loess sequences are terrestrial archives and records of accretionary (e.g., deposition) and degrading near-surface processes (e.g., erosion) (Calitri et al., 2019; Loba et al., 2021; Waroszewski et al., 2018b). Loess and its derived soils are highly susceptible to erosion (Jacobs et al., 2012; Jagercikova et al., 2015; Loba et al., 2021; Waroszewski et al., 2019). The accumulation of loess is favoured by cold and dry climate conditions of former periglacial zones (Gu et al., 1996). It has been speculated that during the main phase of loess deposition, especially during the major glaciations (MIS 2–4, Frechen et al., 2003; Lehmkuhl et al., 2021), loess deposits formed deep mantles which served as a substrate for weak to moderate soil development. Often, these mantles eroded during the Late Pleistocene and Holocene and their residues were

preserved (Döhler et al., 2018; Waroszewski et al., 2018b). As a considerable part of the material has been lost over time, a decrease in soil thickness or even the removal of the whole soil body is expected which gives rise to a strong regression or restart of soil formation (Waroszewski et al., 2018b). Therefore, estimating the thickness of the primary loess mantle helps determining the paleoenvironmental landscape settings and better understanding the landscape transformation during the Pleistocene and the present-day appearance of loess-affected soils (Luehmann et al., 2013; Lorz et al., 2013).

By using meteoric ^{10}Be to determine erosion rates (Chen et al., 2020; Norton et al., 2010; Lal, 2001; Wittmann et al., 2015), changes in the stability of loess cover and soils can be estimated. Once formed in the atmosphere, meteoric ^{10}Be adsorbs onto aerosol particles or is scavenged by rain and deposited on the Earth's surface (Graly et al., 2011; Heikkilä

* Corresponding author.

E-mail address: jaroslaw.waroszewski@upwr.edu.pl (J. Waroszewski).

et al., 2008; Wittmann et al., 2015). Meteoric ^{10}Be easily adheres to fine-grained particles (fine silt, clay) at the soil surface (Arata et al., 2016a, 2016b; Egli et al., 2010; Willenbring and von Blanckenburg, 2010; Wittmann et al., 2015); thus, the highest values are usually found in the uppermost soil horizon (Graly et al., 2011). The penetration depth of ^{10}Be with rainwater primarily depends on the grain size distribution, soil density and adsorption mechanisms in a soil (Willenbring and von Blanckenburg, 2010). The spatial arrangement and profile–depth distribution of meteoric ^{10}Be in soils are controlled by leaching and illuviation processes, as well as by soil mixing (Graly et al., 2011; Waroszewski et al., 2018a). Therefore, meteoric ^{10}Be dynamics in soils indicate the stability and dynamics of loess layers in various ecosystems (Costantini et al., 2018; Drohan et al., 2020; Jary and Kida, 2000; Lehmkuhl et al., 2021; Rousseau et al., 2007; Schatzel et al., 2018; Waroszewski et al., 2018a, 2018b, 2020; Williams, 2015; Yates et al., 2018), and reveal the role of erosion, accumulation, and bioturbation processes.

Because of its unique traits, meteoric ^{10}Be has been typically used as a tracer for erosion and deposition rates in diverse soils under various environmental conditions (e.g., Chen et al., 2020; Marshall et al., 2017; Norton et al., 2010; Lal, 2001; Ritchie and Ritchie, 2007; Wittmann et al., 2015). The calculation of erosion rates based on meteoric ^{10}Be is relatively straightforward. One of the most well-known soil erosion model when using cosmogenic radionuclides (Lal, 2001) assumes steady-state soil conditions and does not take the complex pedosedimentary evolution into account (Waroszewski et al., 2018a,b, Kleber and Terhorst, 2013). Over the last decade, several attempts have been made to calculate the erosion rate of complex heterogeneous soils. For example, Egli et al. (2010) applied a non-steady-state approach to derive the erosion rates in alpine soils. Similarly, Zollinger et al. (2017) applied a non-steady-state approach to determine erosion in soils of alpine

hillslope that developed on unconsolidated sedimentary parent material. Waroszewski et al. (2018b) calculated the long-term erosion for soils formed on stratified slope deposits with airborne dust admixtures exhibiting clear eluviation/illuviation processes in the medium–high mountains of Central Europe. Hidy et al. (2018) used a Monte Carlo simulation and in-situ terrestrial cosmogenic, in-situ nuclides to calculate soil erosion. Furthermore, Arata et al. (2016a,b) introduced a new model for accumulation and erosion rate calculations (MODERN) based on the inventories of fallout radionuclides. Under specific conditions, this model can also be applied to ^{10}Be depth profiles (see Calitri et al., 2019). In loess-dominated areas, soil properties are more homogeneous and, thus, ideal for studying erosional and depositional processes. If the deposition of the loess layer occurred during a well given, single period then the concentrations of meteoric ^{10}Be measured in the C-horizon can be used to calculate the amount of ^{10}Be that derives from a potential pre-exposure.

We now tried to assess soil redistribution rates of complex soil profiles. We had the following main aims: i) the assessment of ^{10}Be migration within loess-bearing heterogeneous soil profiles that are influenced by illuviation, ii) the estimation of long-term erosion rates on soils developed on five different parent materials with a clear loess contribution, and iii) calculation of the original thickness of the loess mantle that is typical for the landscape of Central Europe. We investigated soil profiles that have been developed and reshaped during the Pleistocene and Holocene.

2. Study area

The study area was located in Lower Silesia (southwestern Poland) (Fig. 1). Three regions were selected for this study: i) the Kłodzko Basin, an intramountain depression; ii) the Silesia Massif and iii) the Kaczawa

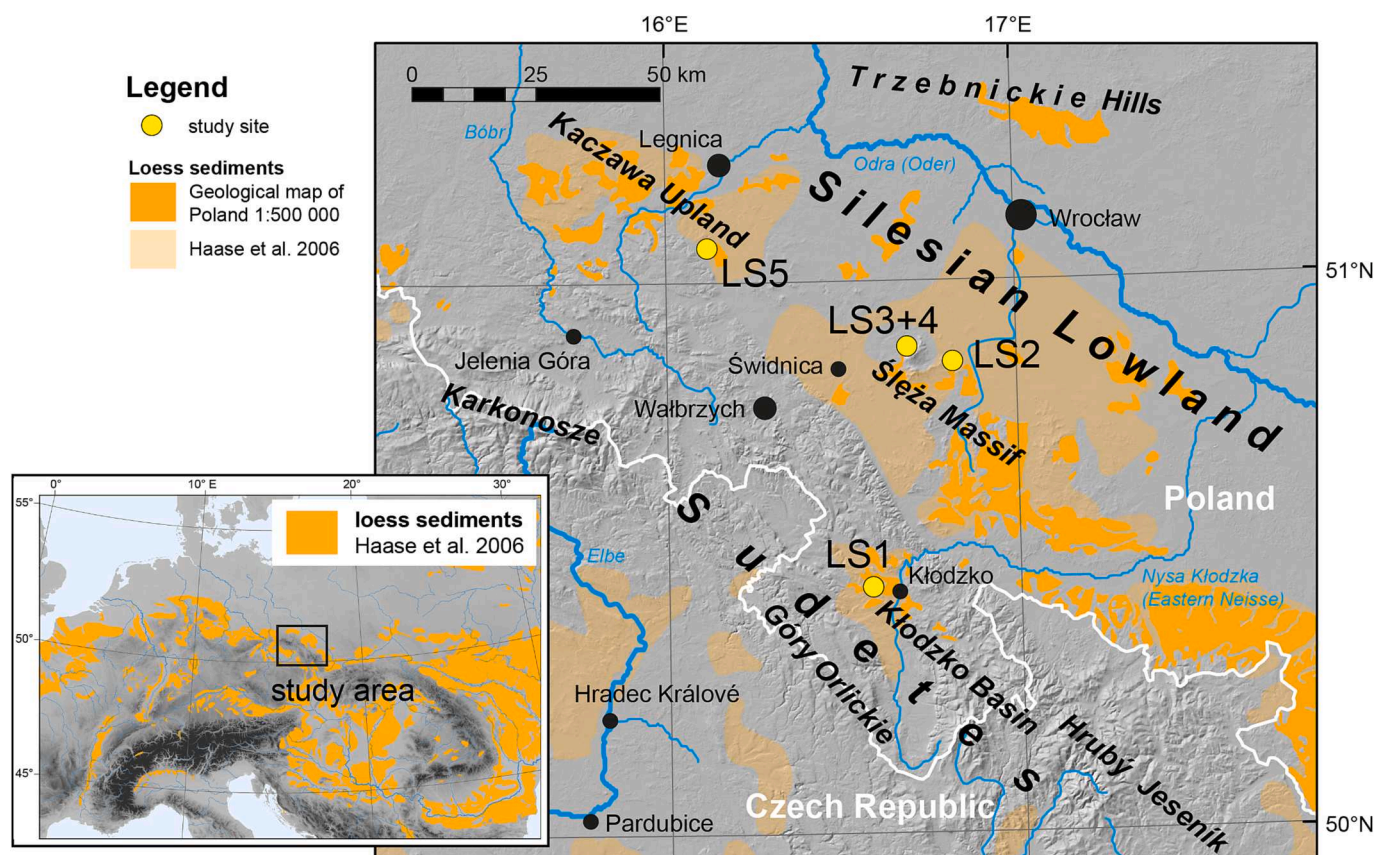


Fig. 1. Location of the studied sites in SW Poland. The loess distribution of Lower Silesia within the European loess belt was drawn after the Geological map of Poland (1:500 000), and Haase et al. (2007) (map of loess sediments in Central Europe adapted from Sprafke 2016, after Haase et al., 2007).

Upland (Kowalska et al., 2022). The Kłodzko Basin comprises Palaeozoic igneous and metamorphic rocks (Wojciechowska, 1966) and Permian sandstone of the Intra-Sudetic Basin (LS1; Awdankiewicz et al., 2003). The Ślęza Massif is subdivided into two geological units, where the first unit constitutes mostly basic to ultrabasic rocks, such as metagabbros, serpentinitised peridotites, ultramafic cumulates, diabases, and metabasalts, the latter predominantly contains Variscan granitoids (Kryza and Pin, 2010; Kierczak et al., 2016). Three soil profiles, LS2, LS3, and LS4, in the Ślęza Massif were investigated, where serpentinite and granite from the Gogołów-Jordanów massif were the basal substrate for soil development for LS2 and LS3 (Dubinska et al., 2010; Gil et al., 2015), while LS4 developed on glaciofluvial sediments. The Kaczawa Upland consists of basalt residual hills, which are remnants of Oligocene–Miocene volcanism that underwent intense and selective denudation during the Pleistocene (Migoń et al., 2020). The products of weathering of the basaltic material act as the geological substrate for LS5.

The origin of loess deposits in Lower Silesia is attributed to both glaciofluvial outwash sediments from the Fennoscandian ice sheet and local sources of the Sudetes (Baykal et al., 2021; Marks, 2005). According to existing chronologies, most of the loess strata of Poland was deposited during the Eemian–Weichselian period MIS5 d-2 (Moska et al., 2019; Valde-Nowak and Lanczont, 2021). However, two major phases with loess sedimentation were established for southwestern Poland, i.e. during MIS 4 and, more notably, MIS 2 (Last Glacial Maximum (LGM 21000 ± 3000 yr; Baykal et al., 2021; Lehmkuhl et al., 2021; Schaffernicht et al., 2020; Moska et al., 2019). During the last glacial cold phases, the Fennoscandian ice sheet reached the southern part of central Europe, thus the main source of dust in the proximal areas is linked with glacial grinding mechanism. This material was easily displaced by wind over long distances (Baykal et al., 2021; Gallet et al., 1998). Most likely easterly winds played a major role in the transfer and deposition of loess in Poland (Schaffernicht et al., 2020). Loess covers are of variable thicknesses, but usually range between 0.3 and 2 m and often form discontinuous patches, with a generally undifferentiated stratigraphy (Jary, 2010). The maximum age of these loess deposits within the study region varies between 17.3 ± 1.1 and 21.0 ± 1.4 ka (Waroszewski et al., 2020, 2021). Only some of the thin loess mantles reveal younger ages (14.2 ± 1.1) (Waroszewski et al., 2020). Because the soils that developed from loess deposits were reworked during the Holocene (e.g., by agriculture, deforestation, and natural processes such as pedoturbation, mass wasting, and slope wash) and probably even during the Late Pleistocene (e.g., by intensive wind erosion or erosive rainfall events during the LGM; Schaffernicht et al., 2020), the primary thickness of the deposited loess remains unknown (Waroszewski et al., 2018a). These processes often reduce the thickness of the loess mantle and favour the mixing of loess material with the underlying substrate (Kleber and Terhorst, 2013; Waroszewski et al., 2018a, 2019).

The soils of Lower Silesia that developed on loess deposits, loess-derived sediments, and within cover sands over glacial tills are usually characterised by illuviation/eluviation processes that form Luvisols (Kabala et al., 2015a,b; Kabala and Musztyfaga, 2016; Waroszewski et al., 2018a; 2019). In other places, a thick humus (mollic) horizon could evolve, resulting in the development of fertile soils such as Chernozems and Phaeozems (Drozd et al., 1994; Drozd et al., 2007; Labaz and Kabala, 2014; Labaz, 2018, 2019; Licznar, 1976). Consolidated ultramafic/mafic rocks, e.g., basalt, serpentinite, or gabbro, are the common parent material for Cambisols or Leptosols (Weber, 1982; Pędziwiatr et al., 2018). Moreover, brunic Arenosols developed on Pleistocene terraces and sand plains, and fluvic Gleysols formed on Holocene river-terraces and occur in Lower Silesia (Kabala et al., 2015a, b).

The recent human land use in Lower Silesia is dominated by arable lands (61%), while forests account for 31%. Main deforestation periods are associated with mining activities of ores such as iron, gold, silver, copper, and lead in the Middle Ages (Kabala et al., 2015a,b).

Anthropogenic disturbances of loess deposits were recently traced by Loba et al. (2021), from the Preboreal to modern times.

Lower Silesia has a temperate climate. South of Lower Silesia, the Sudety Mountains are natural topographic barriers (Bac-Bronowicz and Grzempowski, 2018). The precipitation values differ depending on the region – the mean annual precipitation rate is 750 mm within the Kaczawa Upland and Kłodzko Basin, whereas that in the Ślęza Massif reaches 600 mm (Pawlak, 2008).

The vegetation cover is mostly dominated by a mixed forest, with oak, beech, hornbeam, and spruce as the main species. The Ślęza Massif is partially characterised by a grassland vegetation, with *Alopecurus pratensis* L. and *Festuca rubra* L. (Waroszewski et al., 2019). Additionally, species, such as *Peucedanum cervaria* (L.), *Lapeyr Thesium alpinum* (L.), *Potentilla alba* (L.) and *Drymocalis rupestris* (L.) often overgrow the serpentinite and amphibolite of the Ślęza Massif.

3. Materials and methods

3.1. Soil sampling strategy

Five soil pits from the Lower Silesia province from a previous study (Kowalska et al. 2022) were selected for this investigation: LS1 (Kłodzko Basin), LS2–LS4 (Ślęza Massif) and LS5 (Kaczawa Upland (Fig. 1, Table 1). These soils have developed on different geological substrates (Table 1). Up to three zones of a strongly variable thickness were distinguished among the investigated soils (Waroszewski et al., 2018a): the loess mantle (pure loess material), mixed zone (loess mixed with underlying rocks) and the basal layer (underlying bedrock) (Fig. 2). Waroszewski et al. (2018a, 2019) and Kowalska et al. (2022) provided detailed characteristics of these soils. Prior to sampling, the soil profiles were prepared and described in accordance with the FAO (2006) and IUSS Working Group WRB (2022) guidelines. Soil colour was determined in the field from moist samples using the Munsell Soil Colour Charts. Approximately 2 kg of soil material was collected from each designated horizon for physicochemical and isotopic analyses. The 32 samples were dried at 70 °C and sieved to 2 mm. Additionally, undisturbed samples were collected using steel rings (Kopecky type, 100 cm³) for soil bulk density measurements.

3.2. Particle size distribution, basic chemical and geochemical properties

The method of Van Reeuwijk (2002) was used to estimate particle size distribution which combines sieving (sand fraction) and a hydrometer method (silt and clay fractions). Total organic carbon (TOC) was obtained by dry combustion at 550 °C using a CO₂ spectroscopic detection analyser (Ströhlein CS-mat 5500). The pH was measured potentiometrically in a suspension of 1:2.5 (soil:1 M KCl solution) using an electrode and a CPI-551 Elmetron pH meter (van Reeuwijk, 2002). The sum of exchangeable bases (Ca²⁺, Mg²⁺, Na⁺, and K⁺) was assessed by an extraction of 1 M ammonium acetate at pH 7.0 (van Reeuwijk, 2002). 'Free' iron (Fe_d) was extracted with a bicarbonate–dithionite–citrate buffer. Iron and aluminium in amorphous oxides and hydroxides ('active' forms, Fe_o and Al_o) were extracted using an acid ammonium oxalate solution (Van Reeuwijk, 2002) and measured with ICP-AES (Varian Liberty). The total element concentrations in the fine earth were measured after fusion with lithium borate and an alloy dissolution with nitric acid (Delijaska et al. 1988) using ICP-ES having a Spectro Ciros Vision and ICP-MS (PerkinElmer ELAN 9000 in Acme Labs, Bureau Veritas, Canada).

3.3. Meteoric ¹⁰Be analysis

The meteoric ¹⁰Be content in the fine earth fraction of all soil horizons was analysed following Egli et al. (2010) and Zollinger et al. (2017). Samples were milled using a horizontal mill with tungsten balls at 28 Hz for 10 min. Then, 2 g of the milled sample was weighed and

Table 1
General characteristics of the sampling sites.*.

Profile	Coordinates (N/E)	Elevation (m asl)	Slope inclination (deg)	Slope position	Mean annual precipitation (mm yr ⁻¹)	Geological substrate	Land use	WRB (IUSS Working Group WRB, 2022)
LS1	50°26'05.4"N, 16°34'24.3"E.	529	5	shoulder	750	loess/ Permian sandstone	arable land	Endoskeletal Luvisol (Episiltic, Raptic)
LS2	50°51'20.0"N, 16°46'55.3"E.	250	12	midslope	650	loess/ serpentinite	forest	Endoskeletal Luvisol (Magnesic, Raptic)
LS3	50°52'35.0"N, 16°40'09.1"E.	260	2	summit/ shoulder	650	loess/granite	forest	Katoskeletal Alisol (Raptic)
LS4	50°52'24.6"N, 16°40'09.1"E.	230	3	summit/ shoulder	650	loess/glacio-fluvial deposits	grassland	Endoskeletal Luvisol (Episiltic, Endoloamic, Raptic)
LS5	51°01'10"N, 16°01'40"E.	402	8	backslope	750	loess/ basalt slope cover	forest	Eutric Luvic Albic Folic Stagnosol (Pantosiltic, Ochric,)

Explanations:* according to Kowalska et al., (2022).

ignited at 500 °C for 6 h to remove the organic matter. To extract ¹⁰Be, sample powders were spiked with 1 mg of ⁹Be and leached overnight in 16% HCl. The sample leachate was collected, and the soil samples were leached again to ensure high-efficiency extraction of beryllium. The two leachates were combined, and the fine particles were removed by centrifugation. Metals, including Be dissolved in the leachate, were separated in two stages. In the first stage, liquid samples were treated with NaOH and HCl to separate the metal hydroxides based on the dependency of their solubility on pH, mainly to remove Fe(OH)₃. During pH adjustment, a saturated EDTA solution was added to bind with metals (Fe and Mn) resulting in EDTA complexes for selective separation. The resulting gels of Be, Al, and Ti hydroxides were collected and dissolved in oxalic acid. In the second stage, Be was separated using an ion-exchange resin (Bio Rad AG 50-X8) and collected as Be(NO₃)₂. Finally, the samples were precipitated with NH₄OH, dried, and calcined at 850 °C to obtain pure BeO.

The ¹⁰Be/⁹Be ratio was measured using a MILEA accelerator mass spectrometry (AMS) system at ETH Zurich (Maxeiner et al., 2019). The results were normalized to the ETH AMS standards S2007N (¹⁰Be/⁹Be = 28.1 ± 0.8·10⁻¹²) and S2010N (¹⁰Be/⁹Be = 3.3 ± 0.1·10⁻¹²) both relying on a ¹⁰Be half-life of 1.387 ± 0.012 Myr (Christl et al., 2013). The ¹⁰Be/⁹Be ratio of the samples lied in the range of 1.64·10⁻¹²–14.35·10⁻¹², and the ratio of preparation blanks was 0.011·10⁻¹²–0.021·10⁻¹². The final ¹⁰Be content was corrected to the weighted average of the blank values. Error of the ¹⁰Be content included the errors of the AMS standards and preparation blanks. The error includes the uncertainty of the AMS measurement, including standard normalisation and propagated error of preparation blank subtraction.

3.4. Erosion rate calculations

Information on the approximate start of soil formation is needed to estimate erosion or sedimentation rates. Jary (1999) and Waroszewski et al. (2021) provided the age constraints for loess deposits and their reworking for the Lower Silesia (helped in the calculation of erosion rates. Owing to the assumption of several phases of accumulation and erosion events, steady-state conditions seemed unlikely, as postulated by Lal (2001). Therefore, a non-steady-state approach (Zollinger et al., 2017) was considered to be more suitable for the investigated soils. This approach, however, requires the age of the landform for erosion rate calculations. The precise age of the loess deposits and the onset of soil formation is not known. We, therefore, used a scenario calculation with two different starting points, i.e., 14.2 and 21 ka (Waroszewski et al., 2020, 2021). This age range best designates the loess mantle formation of the region. This approach also requires the annual ¹⁰Be deposition rates as input parameters, which often have to be modelled or estimated. We used again a scenario calculation approach: 1) ¹⁰Be deposition rates estimated using the annual precipitation (Maejima et al., 2005), 2) deposition rates according to Willenbring and von Blanckenburg (2010).

The lowermost samples from all profiles were excluded from the ¹⁰Be inventory, as we intended to focus on the loess component and provide comparable conditions for the loess mantles not affected by the underlying sediment.

Soil erosion was then calculated as (Zollinger et al., 2017):

$$E_{soil} = \frac{1}{\rho f C_{10Be}} \left(\frac{\lambda N}{e^{-\lambda t} - 1} + q \right) \quad (1)$$

where E_{soil} is the soil erosion rate (cm yr⁻¹), C_{10Be} (atoms/g) is the average ¹⁰Be in the top eroding horizons, f is the fine earth fraction, ρ (g/cm³) is the bulk density of the top horizons, N (atoms/cm²) is the ¹⁰Be inventory in the soil profile, q (atoms cm⁻² yr⁻¹) is the annual ¹⁰Be deposition rate, λ (4.997 × 10⁻⁷ yr⁻¹) is the decay constant of ¹⁰Be, and t (y) is the surface age. The average concentrations of ¹⁰Be in rainfall is ~ 1–1.5 × 10⁴ atoms cm⁻³ (see Vonmoos et al., 2006; Heikkilä et al., 2008; Graly et al., 2011).

Although steady-state conditions were not met, the calculation method of Lal (2001) was used for comparison.

$$E_{soil} = z_0 K_E \text{ and (2)}$$

and

$$K_E = \frac{N_D}{N_S} \left[\frac{q}{N_D} \right] - \lambda \quad (3)$$

where z_0 (cm) is the thickness of the topsoil horizons, K_E is the first-order rate constant for the removal of soil from the topsoil layer, N_D (atoms/cm²) is the ¹⁰Be inventory in the D layer (remainder of the soil profile comprising B and C horizons), N_S (atoms/cm²) is the ¹⁰Be inventory in the topsoil horizons, and q (atoms/cm²/yr) is the flux of atmospheric ¹⁰Be onto the topsoil.

Besides soil age, also the average precipitation rates are not precisely known over the entire soil evolution period. While present-day average precipitation rates more or less represent the Holocene, the situation for the Pleistocene is much less known. According to Heyman et al. (2013), annual precipitation was probably 25–75% of the present-day situation during the period of the last glacial maximum. We made an additional scenario calculation by taking these values into account by using:

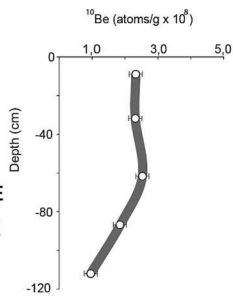
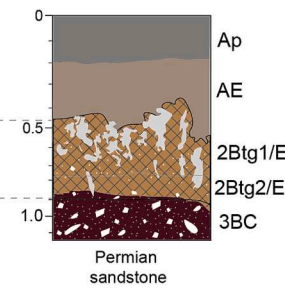
$$P = P_H \times F + P_{IA} \times (1 - F) \quad (4)$$

where P = precipitation rate [mm yr⁻¹] during entire period of soil formation, P_H = precipitation rate during the Holocene, F = precipitation proportionality factor (ratio time of soil evolution during the Holocene to entire duration of soil formation) and P_{IA} = precipitation rate during the Pleistocene (25–75 % of present-days rate).

LS1



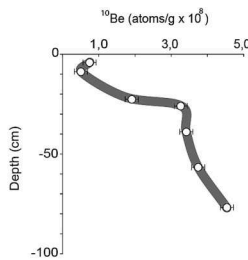
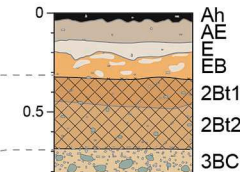
Endoskeletal Luvisol (Episiltic, Raptic)



LS2



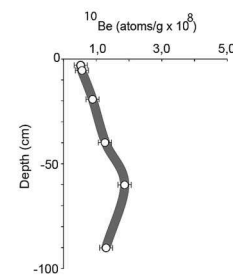
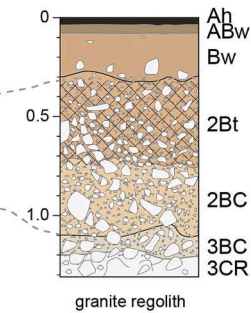
Endoskeletal Luvisol (Magnesic, Raptic)



LS3



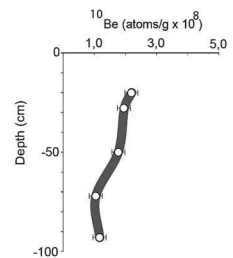
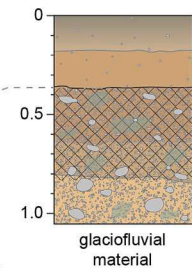
Katoskeletal Alisol (Raptic)



LS4



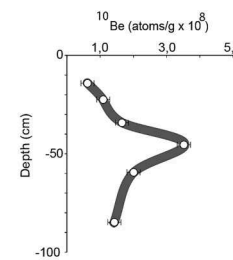
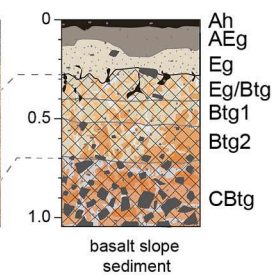
Endoskeletal Luvisol (Episiltic, Endoloamic, Raptic)



LS5



Eutric Luvisol Albic Folic Stagnosol (Pantosiltic, Ochric.)



Legend:

- gravelly
- illuvial clay
- stones (undifferentiated)
- serpentinite
- granite
- sandstone
- lithological boundary
- horizon boundary
- tonguing

Fig. 2. Photos and sketches showing the detailed morphology of all soil profiles and ¹⁰Be depth plots.

4. Results

4.1. Soil morphology and particle size distribution

The investigated soils differed in terms of the geological substrate, land use and location on the slope (Tables 1 and 2). Each profile contained loess material in the topsoil. Usually, three morphological zones were distinguished: loess mantle, mixed zone and basal layer (Table 2). As an exception, soil LS4 had no mixed zones – the dense underlying substrate inhibited a mixing with loess. The loess mantles of most soils were 28–78 cm thick (Table 2), had a silt-loam texture, with a clear predominance of the silt fraction varying from 52% (LS4) to 72% (LS2) (Table 3). The thickest loess mantle (78 cm) was observed in soil LS1 which formed on Permian sandstone (Table 2). Furthermore, the loess mantle contained a relatively low proportion of rock fragments with up to 20% (LS4, Table 2). The rock fragment proportion increased with soil depth in all profiles (Table 2). The basal layers of LS3 and LS5 showed up to 80–85 % of rock fragments in the lowermost horizons. The texture of the mixed zones and basal layers showed an unambiguous decrease in the silt content and an increase in sand (LS1, LS3, and LS4) or clay (LS2,

LS5) (Table 3). Additionally, an argic horizon was found in each soil profile, but at different depths (Table 2). These soils were classified as either Luvisols or Alisols (Table 1). The boundary between the loess and mixed zones was mostly clear and wavy (Table 2). The loess mantles had a very friable consistency, whereas the mixed zones and basal layers were more compact (Table 2). Detailed characteristics of the profiles are presented in Kowalska et al. (2022).

4.2. Physicochemical soil properties

Bulk densities of the different soils were comparable with values of 1.01–1.59 g·cm⁻³ (Table 6). The bulk density of the loess mantle was lower than that of the mixed zone and basal layer (Table 4). The pH values indicate neutral conditions at LS1 and LS2 or acidic conditions at LS3, LS4 and LS5. The values generally increased slightly with soil depth, with some exceptions in LS1 and LS3 where the pH of the basal layers was lower than those of the overlying zones (Table 4). The pH of LS4 soil was more or less uniform along the entire profile. TOC was highest in the Ah horizon of LS3 and LS5 followed by LS2 (Table 4). Profile LS1 had the highest base cation content (23.0–28.1 cmol(+) ·

Table 2
Morphology properties of soils under study.*

Profile	Horizon	Depth (cm)	Coarse fragment	Color (moist)	Redox features	Structure	Consistence (moist)	Horizon boundary	Diagnostics	Texture	Parent material
Endoskeletal Luvisol (Episiltic, Raptic)											
LS1	Ap	0–18	n.d.	10YR 4/2	–	gr, fi	fr	c		SiL	Loess mantle
	AE	18–45	2	10YR 5/4	–	sb, fi	fr	g,w		SiL	
	2Btg1/	45–78	n.d.	10YR 4/6	–	ab, fi	fr/fi	g	argic	SiL	Mixed zone
	E										
	2Btg2/	78–95	25	10YR 6/4	–	ab/pl, fi	fi	c	argic	SiL	
E											
3BC	95–112	60	2.5YR 4/5	–	ab, fi	vfi			SL	Basal layer	
Endoskeletal Luvisol (Magnesic, Raptic)											
LS2	Ah	0–4	n.d.	10YR 3/1	–	gr, vfi	vfr	c,w		SiL	Loess mantle
	AE	4–14	n.d.	10YR 6/3	–	sb, fi	fr	c,w		SiL	
	E	14–19	n.d.	10YR 8/2	–	ab, vfi	fr	g	albic	SiL	Mixed zone
	EB	19–33	n.d.	10YR 6/8	–	ab, fi/m	fi	g	albic	SiCL	
	2Bt1	33–45	40	10YR 4/6	–	ab, fi/m	fi	g	argic	SiCL	
	2Bt2	45–68	50	10YR 4/4	–	ab, fi/m	fi/vfi	g	argic	CL	Basal layer
	3BC	68–86	60	10YR 6/6	–	ab/sb, fi	vfi			SiL	
Katoskeletal Alisol (Raptic)											
LS3	Ah	0–3	5	10YR 2/1	–	gr, vfi	vfr	g		SiL	Loess mantle
	ABw	3–8	5	10YR 4/5	–	sb, fi	fr	g		SiL	
	Bw	8–30	10	10YR 5/6	–	ab, fi	fr	g		SiL	Mixed zone
	2Bt	30–70	40	10YR 6/5	–	ab/pl, m	fr	g	argic	SiL	
	2BC	70–110	60	10YR 6/4	–	ab, m	fr	g		SiL	
	3BC	110–120	70	7.5YR 5/8	–	ab, m	vfr	g		SL	Basal layer
3CR	120–130	85	–	–	–	vfr			SL		
Endoskeletal Luvisol (Episiltic, Endoloamic, Raptic)											
LS4	AE	0–20	5	10YR 5/4	–	sb, fi	fr	w		SiL	Loess mantle
	EB	20–36	20	10YR 5/8	–	sb/ab, fi	fr	g		SiL	
	2Btg1	36–64	60	7.5YR 4/6	2.5 YR 7/3	ab, m	fr/vfr	g	argic	L	Basal layer
	2Btg2	64–81	65	7.5YR 5/6	–	ab/pl, m	vfr	g	argic	SL	
	2BC	81–105	70	5YR 8/3	5Y 8/3–6/3	sb, fi	fr			SCL	
Eutric Luvisol Albic Follic Stagnosol (Pantosiltic, Ochric)											
LS5	O	2–0	n.d.	–	–	–	–	c, w			Loess mantle
	Ah	0–4	10	10YR 2/1	–	sb, fi	vfr	c, w		SiL	
	AEg	4–14	10	10YR 4/1	–	ab, m	fr	c,w		SiL	Mixed zone
	Eg	14–28	16	10YR 7/2	10YR 5/6	ab, m/l	fr	g	albic	SiL	
	Eg/Btg	28–40	30	2.5Y 6/2	10YR 5/8	ab, m/l	fr/fi	g	albic/argic	SiL	
	Btg1	40–50	40	5Y 6/2	10YR 5/6	ab, m	fi	g	argic	SiL	Basal layer
	Btg2	50–70	60	G1 5/5GY	7.5YR 5/8	ab, m	fi	g	argic	CL	
	2CBtg	70–100	80	G1 6/5GY	7.5YR 5/6	ab/sb, m	fi			SiL	

Explanations: structure: vfi – very fine, fi – fine, m – medium, ab – angular blocky, gr – granular, pl – platy, sb – subangular blocky; consistence (moist): vrf – very friable, fr – friable, fi – firm; Horizon boundary: c – clear, g – gradual, s – smooth, w – wavy; texture: SiL – silt loam, CL – clay loam, SCL – sandy clay loam, SL – sandy loam, L – loam, SiCL – silty clay loam; LM – loess mantle, MZ – mixed zone, BL – basal layer; * according to Kowalska et al. (2022).

Table 3
Particle size distribution and density of the studied soils.*.

Profile	Horizon	Depth (cm)	Sand					Silt		Clay fraction <0.002	Sum of fractions		Texture classes USDA
			vcS 2–1	cS 1–0.5	mS 0.5–0.25	fS 0.25–0.1	vfS 0.1–0.05	cSi 0.05–0.02	fSi 0.02–0.002		Sand 2–0.05	Silt 0.05–0.002	
%													
Endoskeletal Luvisol (Episiltic, Raptic)													
LS1	Ap	0–18	0	1	3	5	9	25	40	17	18	65	SiL
LS1	AE	18–45	0	1	3	5	7	27	38	19	16	65	SiL
LS1	2Btg1/E	45–78	0	1	1	2	9	27	35	25	13	62	SiL
LS1	2Btg2/E	78–95	1	3	4	4	8	23	33	24	20	56	SiL
LS1	3BC	95–112	9	16	12	17	8	8	11	19	62	19	SL
LS1	3BC (wedges)	95–112	0	1	1	2	8	29	40	19	12	69	SiL
Endoskeletal Luvisol (Magnesic, Raptic)													
LS2	Ah	0–4	n. d.	n.d.	n.d.	n.d.	n.d.	n.d.	n.d.	n.d.	n.d.	n.d.	n.d.
LS2	AE	4–14	0	1	2	2	14	36	36	9	19	72	SiL
LS2	E	14–19	1	2	2	2	15	34	33	11	22	67	SiL
LS2	EB	19–33	1	2	1	1	17	26	27	25	22	53	SiL
LS2	2Bt1	33–45	0	1	3	4	10	25	29	28	18	54	SiCL
LS2	2Bt2	45–68	0	1	4	4	10	25	28	28	19	53	SiCL
LS2	3BC	68–86	0	1	3	5	22	15	25	29	31	40	CL
Katoskeletal Alisol (Raptic)													
LS3	Ah	0–3	3	3	8	9	10	39	22	6	33	61	SiL
LS3	ABw	3–8	1	2	4	4	10	40	33	6	21	73	SiL
LS3	Bw(t)	8–30	1	2	3	5	8	34	35	12	19	69	SiL
LS3	2Bt	30–50	2	2	3	4	7	35	34	13	18	69	SiL
LS3	2BC	50–70	4	3	5	5	9	32	30	12	26	62	SiL
LS3	3BC	70–110	21	17	16	12	9	7	10	8	75	17	SL
LS3	3CR	110–130	32	15	10	9	6	8	15	5	72	23	SL
Endoskeletal Luvisol (Episiltic, Endoloamic, Raptic)													
LS4	AE	0–20	1	2	4	4	13	30	38	8	24	68	SiL
LS4	EB	20–36	1	3	6	8	11	27	25	19	29	52	SiL
LS4	2Btg1	36–64	3	8	8	13	8	10	24	26	40	34	L
LS4	2Btg2	64–81	5	14	20	19	5	7	12	18	63	19	SL
LS4	2BC	81–105	7	14	11	12	7	5	19	25	51	24	SCL
LS4	2BC (wedges)	81–105	3	8	10	13	10	13	21	22	44	34	CL
Eutric Luvisol Albic Follic Stagnosol (Pantosiltic, Ochric.)													
LS5	Ah	0–4	n. d.	n.d.	n.d.	n.d.	n.d.	n.d.	n.d.	n.d.	n.d.	n.d.	n.d.
LS5	AEg	4–14	1	4	5	5	6	29	42	8	21	71	SiL
LS5	Eg	14–28	2	5	5	4	9	30	34	11	25	64	SiL
LS5	Eg/Btg	28–40	1	4	5	5	6	25	30	24	21	55	SiL
LS5	Btg1	40–50	1	2	5	5	7	24	32	24	20	56	SiL
LS5	Btg2	50–70	1	3	4	4	7	24	35	22	19	59	SiL
LS5	2CBtg	70–100	1	5	8	11	7	14	24	30	32	38	CL

Explanations: n.d. – not determined; * according to Kowalska et al. (2022).

kg⁻¹) and exchangeable Ca (13.6–18.4 cmol(+) · kg⁻¹). Such a high calcium content may have been the result of past cultivation. The soils LS4 and LS5, which developed on glaciofluvial sediments and a basalt slope cover, exhibited a heterogeneous basic cation content along the soil profile (2.72–27.6 cmol(+) · kg⁻¹). The vertical distribution of dithionite-extractable Fe (Fe_d) was highly variable. The highest Fe_d content was observed in soils LS1 and LS5 (Table 4). Interestingly, the Fe_d content increased with increasing soil depth. Soil LS2 and LS4 were depleted in Fe_d in the E and 2Btg2 horizons, respectively. The 2Bt horizon of soil LS3 was enriched in Fe_d (Table 4). More heterogeneous values were measured with the oxalate-extractable Fe and Al (Fe_o and Al_o). However, a slight accumulation of Fe_o was noted in the subsoils, e. g., horizons 2Bt1 of LS2, EB of LS4, and Eg/Btg and Btg1 of LS5 (Table 4). The soils LS3 and LS5 showed a decrease in Al_o with increasing soil depth, whereas the horizons 2Btg1/E, E and 2Btg1 of LS1, LS2, and LS4, respectively, showed a slight accumulation of Al_o (Table 4).

4.3. Soil geochemistry

The Hf and Zr contents in the loess mantle and mixed zone of LS1, LS2 and LS3 always exceeded 8 and 237 mg·kg⁻¹, respectively (Table 5), suggesting the presence of an aeolian silt admixture (Scheib et al., 2014; Waroszewski et al., 2018a). In soil LS4, only the loess mantle showed clear aeolian signatures because the basal layer exhibited lower values for Hf and Zr (1.3–3.3 and 39.9–118.7 mg·kg⁻¹, respectively). An aeolian silt admixture was potentially present along the whole soil profile of LS5, where the Hf and Zr contents were 10.6–13.0 and 381.0–481.5 mg·kg⁻¹, respectively (Table 5). All soils were characterised by a moderate to high SiO₂ content (50.8–83.1 %, Table 5). Generally, SiO₂ decreased with soil depth while Al₂O₃ increased. The mixed zone and the basal layer of LS4 had a relatively high Fe₂O₃ content compared to the other soils 5.02–8.86 wt% (Table 5). Furthermore, the MgO content was much higher in LS2 than in the other profiles (1.25–6.23 wt%), particularly in the basal layer. LS4 exhibited relatively

Table 4
Selected chemical properties of the investigated soils.*.

Profile	Horizon	Depth (cm)	TOC (%)	pH H ₂ O	Ca cmol(+) kg ⁻¹	Mg kg ⁻¹	K	Na	S g kg ⁻¹	BS (%)	Fe _d	Fe _o	Al _o	Fe _o /Fe _d
Endoskeletal Luvisol (Episiltic, Raptic)														
LS1	Ap	0–18	1.57	6.44	17.6	1.73	0.97	0.52	27.3	n.d.	0.80	0.23	0.06	0.28
	AE	18–45	1.22	6.3	16.0	1.52	0.64	0.49	25.0	n.d.	0.81	0.14	0.05	0.18
	2Btg1/E	45–78	0.29	7.35	18.4	2.06	0.3	0.57	28.1	n.d.	1.12	0.20	0.08	0.18
	2Btg2/E	78–95	1.18	7.15	16.0	2.74	0.3	0.52	27.1	n.d.	1.03	0.19	0.07	0.19
	3BC	95–112	0.13	6.01	14.4	2.99	0.32	0.49	23.5	n.d.	1.27	0.07	0.04	0.06
	3BC (wedges)	95–112	0.18	7.57	13.6	1.64	0.18	0.46	23.0	n.d.	n.d.	n.d.	n.d.	n.d.
Endoskeletal Luvisol (Magnesic, Raptic)														
LS2	Ah	0–4	2.39	4.24	9.53	6.06	0.71	0.69	16.9	n.d.	0.65	0.27	0.10	0.41
	AE	4–14	1.88	4.5	0.97	1.65	0.12	0.45	3.19	n.d.	0.73	0.28	0.09	0.38
	E	14–19	0.63	4.8	0.62	2.36	0.13	0.50	3.61	n.d.	0.41	0.29	0.19	0.71
	EB	19–33	0.36	4.79	1.05	2.16	0.26	0.57	4.03	n.d.	0.65	0.23	0.08	0.35
	2Bt1	33–45	0.38	5.96	0.80	2.60	0.37	0.60	4.37	n.d.	0.77	0.40	0.09	0.52
	2Bt2	45–68	0.22	6.28	0.56	2.26	0.38	0.54	3.74	n.d.	0.87	0.26	0.11	0.3
	3BC	68–86	0.24	6.43	0.87	3.61	0.40	0.59	5.47	n.d.	n.d.	0.28	0.10	n.d.
Katoskeletal Alisol (Raptic)														
LS3	Ah	0–3	5.71	4.02	2.22	0.85	0.39	0.22	3.70	n.d.	0.18	0.16	0.19	0.91
	ABw	3–8	4.51	4.38	1.76	0.56	0.23	0.18	2.70	n.d.	0.35	0.29	0.17	0.84
	Bw(t)	8–30	1.19	4.49	1.44	0.47	0.11	0.09	2.10	n.d.	0.34	0.17	0.17	0.51
	2Bt	30–50	0.67	4.61	1.28	0.46	0.10	0.09	1.90	n.d.	0.85	0.12	0.13	0.14
	2BC	50–70	0.34	4.53	0.96	0.25	0.13	0.08	1.40	n.d.	0.37	0.06	0.10	0.17
	3BC	70–110	0.31	4.28	1.12	0.50	0.12	0.08	1.80	n.d.	0.43	0.05	0.12	0.1
	3CR	110–130	0.24	4.08	0.96	0.48	0.13	0.09	1.70	n.d.	0.54	0.02	0.10	0.04
Endoskeletal Luvisol (Episiltic, Endoloamic, Raptic)														
LS4	AE	0–20	1.02	5.3	4.72	1.09	0.17	0.19	6.18	87	0.43	0.27	0.11	0.62
	EB	20–36	0.39	5.3	7.52	1.66	0.15	0.26	9.59	90	0.51	0.35	0.12	0.69
	2Btg1	36–64	0.18	5.32	16.0	5.29	0.12	0.39	21.8	91	0.89	0.17	0.15	0.19
	2Btg2	64–81	0.08	5.22	8.4	4.09	0.11	0.29	12.8	90	0.49	0.10	0.08	0.21
	2BC	81–105	0.09	5.2	12.8	5.77	0.09	0.42	19.0	96	0.85	0.13	0.09	0.15
	2BC (wedges)	81–105	0.13	5.3	18.4	7.48	0.11	0.51	26.5	96	0.68	0.13	0.10	0.19
Eutric Luvisol Albic Follic Stagnosol (Pantosiltic, Ochric)														
LS5	Ah	0–4	3.43	5.3	15.2	9.67	2.34	0.46	27.6	95	n.d.	n.d.	n.d.	n.d.
	AEg	4–14	2.56	3.76	1.60	0.79	0.12	0.21	2.72	36	0.67	0.21	0.07	0.32
	Eg	14–28	0.39	4.23	2.24	1.96	0.11	0.23	4.54	58	0.96	0.21	0.07	0.22
	Eg/Btg	28–40	0.19	4.57	5.92	6.99	0.20	0.35	13.4	89	1.04	0.34	0.07	0.33
	Btg1	40–50	0.29	4.58	7.36	9.08	0.26	0.37	17.0	92	1.98	0.34	0.07	0.17
	Btg2	50–70	0.14	5.16	7.60	9.61	0.23	0.44	17.8	99	0.87	0.19	0.05	0.22
	2CBtg	70–100	0.16	5.42	9.60	14.02	0.21	0.52	24.3	99	1.35	0.21	0.05	0.16

Explanations: Note: TOC – soil organic carbon, BS – base saturation, Fe_o/Al_o – oxalate extractable Fe/Al, Fe_d/Al_d – dithionite extractable Fe/Al; * according to Kowalska et al., (2022).

high values of MgO, CaO and Na₂O (Table 5). In the soils LS1, LS2 and LS3, the K₂O and TiO₂ contents generally increased with depth whereas in soils LS4 and LS5, an opposite trend was observed (Table 5).

4.4. Meteoric ¹⁰Be contents and soil erosion rates

4.4.1. Meteoric ¹⁰Be in the soil profiles

The ¹⁰Be contents ranged from 0.52×10^8 (horizon Ah of soil LS3) to 4.54×10^8 atoms g⁻¹ (horizon 3BC of LS2). The content and distribution of meteoric ¹⁰Be varied with different patterns along the profiles. In profiles LS2 and LS3, ¹⁰Be increased with soil depth, becoming maximum in the BC horizon (Table 6, Fig. 2), whereas LS1 and LS4 showed the opposite trend (Table 6). However, a slight increase in ¹⁰Be was observed in horizon 2Btg1/E of soil LS1 (2.53×10^8 atoms g⁻¹, Fig. 2) and 2BC of LS3 (1.87×10^8 atoms g⁻¹, Fig. 2). A different trend was detected in profile LS5, where ¹⁰Be content generally increased with soil depth, reaching 3.55×10^8 atoms g⁻¹ (Fig. 2) in the Btg1 horizon, and then decreased towards the bottom of the soil profile. Similar to soils LS1 and LS3, a clear accumulation of ¹⁰Be in horizon Btg1 of LS5 horizon was noted. Except for profiles LS1 and LS4, other soils showed depletion of ¹⁰Be in the topmost horizons.

4.4.2. Soil erosion rates using ¹⁰Be

Several procedures were applied to calculate the erosion rates (Section 3.5). Irrespective of the approach used, the highest rates were obtained for soil LS3. Depending on the assumed soil age and precipitation rates, the erosion rates varied greatly from 0.11 to 3.27 t ha⁻¹ yr⁻¹). LS1 and LS2 had the lowest erosion rates. Usually, higher erosion rates were obtained using the approach of Lal (2001) and the indifferent deposition rates over time according to Willenbring and von Blanckenburg (2010) (Table 7). The lowest erosion rates were obtained using the approach Zollinger et al. (2017), a soil age of about 14kyr and a low precipitation (25% of the Holocene rates) during the late Pleistocene. As a consequence, the removed loess layer varied greatly between about 1 dm up to about greater than 6 m (Table 7). A removal of loess material more than 6 m, however, seems rather unlikely.

In addition, as soil formation must have started after the LGM and Oldest Dryas when climate was more favourable (Malkiewicz et al., 2016; Waroszewski et al., 2020) and when no additional aeolian sediments were deposited, the rates calculated using a soil age of 14 kyr seem to be more realistic. The removed loess over the entire period of soil formation accounts for a few dm to about 3 m.

Table 5
Content of major and selected trace elements (Hf and Zr).*

	SiO ₂ (%)	Al ₂ O ₃	Fe ₂ O ₃	MgO	CaO	Na ₂ O	K ₂ O	TiO ₂	P ₂ O ₅	MnO	Cr ₂ O ₃	Hf mg·kg ⁻¹	Zr	Rb	
Endoskeletal Luvisol (Episiltic, Raptic)															
LS1	Ap	76.6	8.6	2.62	0.62	0.65	0.82	2.49	0.73	0.18	0.08	0.009	14.3	533.2	84.40
	AE	77.4	8.74	2.63	0.61	0.59	0.84	2.49	0.74	0.16	0.09	0.009	15.1	558.7	84.60
	2Btg1/E	74.7	10.5	3.68	0.87	0.68	0.78	2.56	0.77	0.09	0.05	0.011	12.4	517.7	97.30
	2Btg2/E	74.3	10.7	3.90	0.93	0.62	0.87	2.69	0.73	0.10	0.04	0.011	10.7	407.1	101.1
	3BC	70.6	13.6	3.48	1.05	0.35	1.57	4.17	0.39	0.06	0.04	0.005	5.40	186.5	167.8
Endoskeletal Luvisol (Magnetic, Raptic)															
LS2	AE	79.7	6.36	2.24	1.50	0.43	0.90	1.99	0.72	0.04	0.03	0.040	15.6	605.3	56.7
	E	80.3	7.12	2.80	1.55	0.42	0.87	2.12	0.76	0.04	0.05	0.048	17.6	656.2	62.0
	EB	75.5	9.68	3.97	1.35	0.34	0.78	2.36	0.73	0.06	0.05	0.036	13.3	491.3	80.3
	2Bt1	72.6	10.2	5.17	2.26	0.33	0.81	2.22	0.73	0.06	0.07	0.065	12.8	487.6	82.9
	2Bt2	71.8	9.97	5.29	3.17	0.38	0.82	2.10	0.69	0.04	0.09	0.076	11.1	421.0	78.3
	3BC	67.0	9.16	6.67	6.23	0.34	0.61	1.64	0.57	0.02	0.10	0.155	7.60	292.6	70.2
Katoskeletal Alisol (Raptic)															
LS3	ABw	79.1	6.38	1.66	0.25	0.29	0.81	1.96	0.68	0.05	0.02	0.008	13.5	504.0	59.20
	Bw1 (t)	82.3	7.24	1.80	0.31	0.31	0.87	2.09	0.70	0.03	0.04	0.009	13.5	521.7	58.40
	2Bt	82.7	7.64	1.90	0.36	0.32	0.93	2.27	0.70	0.03	0.03	0.008	13.4	509.5	67.00
	2BC	82.0	8.10	1.99	0.42	0.32	1.09	2.46	0.67	0.02	0.03	0.009	13.2	509.9	74.20
	3BC	71.1	14.9	2.22	0.42	0.09	3.66	3.68	0.47	0.03	0.02	0.004	5.70	200.4	107.1
	3CR	65.2	18.5	2.70	0.51	0.05	3.90	4.54	0.50	0.03	0.01	0.002	5.20	152.8	158.0
Endoskeletal Luvisol (Episiltic, Endoloamic, Raptic)															
LS4	AE	79.2	8.21	2.38	0.50	0.53	0.92	2.32	0.72	0.08	0.11	0.010	13.6	493.8	73.2
	EB	78.2	9.27	3.21	0.64	0.52	0.84	2.25	0.67	0.05	0.05	0.012	11.8	457.0	75.7
	2Btg1	58.7	17.1	7.88	2.03	2.03	0.66	1.29	0.70	0.03	0.05	0.041	3.3	118.7	43.8
	2Btg2	69.9	13.1	5.02	0.89	1.01	1.15	1.85	0.64	0.03	0.06	0.017	2.6	84.80	61.7
	2BC	57.7	18.6	7.49	1.18	1.58	1.39	2.04	1.14	0.03	0.12	0.034	2.0	50.60	61.6
	2BC (wedges)	50.7	21.1	8.86	2.29	2.68	0.75	0.98	0.79	0.01	0.13	0.069	1.3	39.90	30.7
Eutric Luvisol Albic Folic Stagnosol (Pantosiltic, Ochric)															
LS5	Eg	83.0	7.23	1.82	0.38	0.44	0.9	2.16	0.8	0.07	0.02	0.01	13.0	481.5	89.1
	Eg/Btg	75.9	9.76	4.11	0.74	0.53	0.87	2.16	0.8	0.04	0.04	0.014	10.0	381.7	86.3
	Btg1	74.7	10.4	3.78	0.86	0.58	0.85	2.27	0.82	0.05	0.03	0.015	12.0	432.2	76.9
	2CBtg	64.7	12.9	7.38	1.34	0.91	0.74	1.8	1.35	0.13	0.14	0.034	10.6	403.5	74.9

Explanations:* according to Kowalska et al., (2022).

5. Discussion

5.1. Distribution of meteoric ¹⁰Be in polygenetic soils on different basal substrates

Atmospheric ¹⁰Be in loess-bearing slope deposits was variably distributed with irregular profile patterns (Fig. 2). The content of meteoric ¹⁰Be in the loess mantles of the soils was relatively low (0.61–2.33 × 10⁸ atoms cm⁻², Table 6) when compared to other areas having similar setting (Jagercikova et al., 2015). However, as the loess deposits in the study area are relatively young (14.2–23.0 ka) (Warszewski et al., 2020, 2021) the concentrations of ¹⁰Be are in the expected range. Moreover, the studied soil profiles on the slope were constantly subjected to mixing and redistribution. Thus, they often show a distinct variability and irregular distribution of meteoric ¹⁰Be with depth (Table 6). Also, pedogenic processes, such as eluviation and illuviation greatly favour intra-site differences of the ¹⁰Be distribution (Willenbring and von Blanckenburg, 2010).

Once deposited from atmosphere, ¹⁰Be atoms reach the soil surface and firmly attach to fine particles such as clay and soil organic material (Boschi and Willenbring, 2021; Graly et al., 2011; Willenbring and von Blanckenburg, 2010) as these fractions offer a large surface area for meteoric ¹⁰Be adsorption (Chen et al., 2020; Maejima et al., 2005; Wallbrink and Murray, 1994). Atmospheric ¹⁰Be may then undergo vertical translocation via illuviation (Jagercikova et al., 2015; Warszewski et al., 2018b). This phenomenon was observed in all soils with active leaching (LS2, LS3, and LS5; Fig. 2). In both cases, an enrichment

of ¹⁰Be was detected in the subsoil (horizons 2BC and 2Btg1 in soils LS3 and LS5, respectively, Fig. 2), indicating that at least part of ¹⁰Be was translocated through clay illuviation which is typical for Luvisols (Calitri et al., 2019; Marquard et al., 2019).

A different distribution of meteoric ¹⁰Be was noted in LS1 and LS4, where its content decreased from the topsoil to the subsoil (Fig. 2). A slight influence of clay migration was observed as the ¹⁰Be content weakly increased in the 2Btg1/E horizon (Fig. 2). The deposition of aeolian silt particles progressively formed a thick loess mantle on the land surface (0–78 cm, Table 2), which favoured the surface accumulation of meteoric ¹⁰Be (Wyshnytzky et al., 2015). Similar trends of ¹⁰Be have also been reported for some soils of the Karkonosze Mountains (southwest Poland, Warszewski et al., 2018b) and the Gordon Gulch (Colorado, USA, Wyshnytzky et al., 2015). However, this pattern suggests an earlier stage of pedogenesis, where the majority of ¹⁰Be atoms have not yet been translocated by clay particles or recent accumulation of aeolian silt. Alternatively, the decreasing contents of meteoric ¹⁰Be in the subsoil might be a result of the relative increase in the sand fraction (Fig. 2, Table 3) (Chen et al., 2020; Shen et al., 2004) because sand grains have a much lower ¹⁰Be adsorption capacity (Aldahan et al., 1999; Chen et al., 2020). Considering the position of LS1 on the slope (shoulder, Table 1), the addition of meteoric ¹⁰Be-enriched soil material from upslope due to downslope transport may have significantly increased the total Be inventory (Marquard et al., 2019; Wyshnytzky et al., 2015).

The highest concentration of ¹⁰Be at LS4 was detected in the loess mantle (2.20 and 1.97 × 10⁸ atoms/g in the AE and EB horizons,

Table 6
Atmospheric ¹⁰Be concentrations and errors of the different profiles.

Profile	Horizon	Depth (cm)	Bulk density (g·cm ⁻³)	Fine earth weight (g·cm ⁻²)	¹⁰ Be (10 ⁸ at g ⁻¹)	Soil skeleton (%)	¹⁰ Be per horizon (10 ⁸ at cm ⁻²)	Error (%)
LS1	Ap	0-18	1.35	24.3	2.33 ± 0.07	0	27.15	2.90
	AE	18-45	1.23	33.2	2.31 ± 0.07	2	35.79	2.92
	2Btg1/E	45-78	1.28	42.2	2.53 ± 0.07	0	27.86	2.92
	2Btg2/E	78-95	1.48	25.1	1.87 ± 0.05	25	6.19	2.92
	3BC	95-112	1.57	26.7	0.96 ± 0.03	60	0.00	2.90
LS2	Ah	0-4	0.85	3.4	0.75 ± 0.02	0	2.56	2.96
	AE	4-14	1.18	11.8	0.52 ± 0.02	0	6.19	3.05
	E	14-19	1.23	6.1	1.74 ± 0.05	0	3.28	2.92
	EB	19-33	1.36	19.0	3.29 ± 0.10	10	35.58	2.92
	2Bt1	33-45	1.45	17.4	3.41 ± 0.10	40	23.01	2.90
	2Bt2	45-68	1.49	34.3	3.74 ± 0.11	60	0.00	2.90
	3BC	68-86	1.53	27.5	4.54 ± 0.13	75	0.00	2.90
LS3	Ah	0-3	0.97	2.91	0.52 ± 0.02	5	1.45	2.99
	ABw	3-8	1.01	5.05	0.55 ± 0.02	5	2.66	2.95
	Bw(t)	8-30	1.29	28.3	0.88 ± 0.03	10	22.49	3.32
	2Bt	30-50	1.44	28.8	1.28 ± 0.04	40	1.27	2.93
	2BC	50-70	1.55	31.0	1.87 ± 0.05	60	8.13	2.90
	3BC	70-110	1.43	57.2	1.29 ± 0.04	70	0.00	2.90
LS4	AE	0-20	1.22	24.40	2.20 ± 0.06	5	22.98	2.90
	EB	20-36	1.31	20.96	1.97 ± 0.06	20	12.66	2.90
	2Btg1	36-64	1.46	42.34	1.77 ± 0.05	70	7.15	2.90
	2Btg2	64-81	1.35	22.95	1.05 ± 0.03	70	7.20	2.90
	2BC	81-105	1.41	33.84	1.17 ± 0.03	70	0.00	2.90
LS5	AEg	4-14	1.27	12.70	0.61 ± 0.02	10	7.01	3.00
	Eg	14-28	1.34	18.76	1.02 ± 0.03	15	16.24	3.40
	Eg/Btg	28-40	1.41	16.92	1.64 ± 0.05	30	5.13	2.90
	Btg1	40-50	1.47	29.40	3.55 ± 0.10	60	27.47	2.92
	Btg2	50-70	1.51	30.20	1.99 ± 0.06	80	4.64	2.92
	2CBtg	70-100	1.59	47.70	1.42 ± 0.04	80	0.00	2.93

Explanations: erosion = positive values; accumulation = negative values. ¹⁾ equation according to Zollinger et al., (2017) based on the mean precipitation (mm/y) at the studied area; ²⁾ equation according to Zollinger et al., (2017) based on the minimum precipitation (mm/y) at the studied area; ³⁾ equation according to Zollinger et al., (2017) based on the maximum precipitation (mm/y) at the studied area; ⁴⁾ equation according to Zollinger et al., (2017) based on the mean precipitation (mm/y) at the studied area and the annual deposition rate according to Willenbring and von Blanckenburg (2010); ⁵⁾ equation according to Lal (2001). The erosion rates were calculated for an expected soil age of 21 ka for the studied area (Waroszewski et al., 2020); 6) the removed loess layer was calculated based on the approximate age of soil (Waroszewski et al., 2021) and the equation according to Zollinger et al., (2017) based on the mean precipitation (mm/y) at the studied area.

Table 7
Estimated soil erosion rates based on scenario calculations: a) assuming a soil age of 14 kyr (Waroszewski et al., 2020, 2021) or b) a soil age of 21 kyr (Waroszewski et al., 2020, 2021) and derived removal of the loess over the entire period.

Soil age	C1: Erosion rates (t ha ⁻¹ yr ⁻¹)				C2: Erosion rates (t ha ⁻¹ yr ⁻¹)				C3: Erosion rates (t ha ⁻¹ yr ⁻¹)				Overall min. and max. erosion rates (t ha ⁻¹ yr ⁻¹)				Removed of loess layer (m)			
	14 ka		21 ka		14 ka		21 ka		14 ka		21 ka		14 ka		21 ka		14 ka		21 ka	
	Min	Max	Min	Max	Min	Max	Min	Max	Min	Max	Min	Max	Min	Max	Min	Max	Min	Max	Min	Max
LS1	0.11	0.25	0.21	0.57	0.61	1.03	0.70	0.78	0.54	0.72	0.11	0.78	0.21	1.03	0.12	0.86	0.34	1.68		
LS2	0.32	0.42	0.31	0.56	0.68	0.90	0.62	0.69	0.48	0.64	0.32	0.69	0.31	0.90	0.42	0.90	0.60	1.74		
LS3	1.88	2.17	1.54	2.27	2.95	3.27	1.83	2.01	1.41	1.87	1.83	2.95	1.41	3.27	2.38	3.84	2.72	6.30		
LS4	0.78	0.93	0.67	1.05	1.34	1.58	1.10	1.21	0.84	1.12	0.78	1.34	0.67	1.58	0.83	1.43	1.06	2.49		
LS5	0.67	0.83	0.60	1.00	1.24	1.53	1.46	1.61	1.12	1.49	0.67	1.61	0.6	1.53	0.71	1.71	0.94	2.40		

Erosion = positive values; accumulation = negative values.
 C1) Calculation according to Zollinger et al., (2017) and using 25% (min.) and 75% (max.) of Holocene’s annual precipitation during the Pleistocene (Heyman et al., 2013).
 C2) Calculation according to Zollinger et al., (2017) and annual deposition rates (indifferent over time) according to Willenbring and von Blanckenburg (2010); and using 25% (min.) and 75% (max.) of Holocene’s annual precipitation during the Pleistocene (Heyman et al., 2013).
 C3) Calculation according to Lal (2001).

respectively). Although the soil LS4 had a well-developed Bt horizon, ¹⁰Be gradually decreased with depth. Unlike soils LS3 and LS5, there was no enrichment of meteoric ¹⁰Be in the subsoil (Bt horizon) owing to illuviation. Considering the morphology of soil LS4 (Table 2) and the lack of a mixed zone, it was assumed that the material (loess and glaciofluvial sediments) was not sufficiently mixed; therefore, the source of

the ¹⁰Be in the basal layer remains unknown. We hypothesised that i) the friable or very friable consistency (Table 2) of soil LS4 may have favoured an easy displacement of meteoric ¹⁰Be and its final presence even in the deepest layers of the soil (Wyshnytzky et al., 2015) or ii) the high ¹⁰Be content is due to the exposure of the basal layer for a long time prior to being covered by loess (pre-exposure and, thus, inheritance).

Consequently, the upper part of soil LS4 might have started to accumulate atmospheric ^{10}Be after the LGM.

The meteoric ^{10}Be content at LS2 did not decrease with depth (Table 6). Its high values at the bottom of LS2 ($3.41\text{--}4.54 \times 10^8$ atoms/g, Fig. 2, Table 6) suggest that the serpentinite slope deposits are an old paleo-surface exposed to cosmogenic isotope accumulation for a longer period. Since the majority of the loess in the area of Lower Silesia was deposited during the Last Glacial period (Waroszewski et al., 2020), the deposition of meteoric ^{10}Be on the uncovered serpentinite regolite must have started much earlier.

We assumed that the former well-developed upper loess mantle of LS2 (Table 7) was redeposited and eroded, resulting at a later stage in the development of a Luvisol. Loess was probably added during reworking and mixing on the slope, leading to the loss or displacement of a significant part of ^{10}Be into the mixing zone (Yang et al., 2020). It seems rather unlikely that loess influenced the entire ^{10}Be distribution along the profile, as no other signs indicated the same (neither the grain size distribution nor the Hf and Zr contents, Table 5). It cannot be ruled out that part of ^{10}Be was translocated by illuviation because an argic horizon was recognised in LS2 (Table 2). The slight increase in the clay content (Table 3) and Fe_d (Table 4) towards the bottom may suggest leaching during pedogenesis (Gu et al., 1996; Marquard et al., 2019). This assumption is supported by the relatively low pH values within the loess mantle and mixed zone of LS2 (4.2–4.8, Table 4) (Gu et al., 1996).

5.2. Erosion rates of loess-mantled soils

It is difficult to unambiguously estimate long-term soil erosion rates of soils developed on highly reworked slopes. Although the soils were located in one region (Fig. 1), the range of the obtained erosion rates was relatively high and depended on the assumed environmental parameters (Table 7). The long-term erosion rates were partially within the range of tolerable erosion rates for European soils ($0.3\text{--}1.4 \text{ t ha}^{-1} \text{ yr}^{-1}$, Verheijen et al., 2009 and references therein). The steepest slopes were expected to exhibit the highest erosion rates (and the lowest meteoric ^{10}Be content) (e.g., Puchol et al., 2014). However, the calculated long-term erosion rates were not always consistent with the relief (Table 1). Furthermore, the hillslope position may greatly influence erosion rates. It was assumed that the shoulder and back slope were subject to the greatest erosion rates, whereas the summit position has the least erosion (Vanini and Amini, 2017). The highest soil erosion rates were measured at the summit/shoulder of the slope (LS3, LS4, Table 7), where inclination was low ($2\text{--}3^\circ$, Table 2). Surprisingly, it decreased in the middle- and back-slopes (LS5 and LS2), which were characterised by a higher inclination (especially at LS2, Table 7) compared to the other sites. This contradicts other studies, e.g., Loba et al. (2021).

The high erosion rates at LS3 and LS4 were also reflected by the calculated loss of the loess mantles with 0.8 to 3.8 m, respectively (Table 7; 14 kyr). The loess cover at these sites is currently ~ 40 cm thick (Table 2). Regardless of the calculation model used, the estimated erosion rates were highest for soil LS3 (and soil LS4, Table 7). The highest long-term erosion rates for LS3 were surprising because, for over three centuries, this site has been covered by a forest that should have increased the resistance to erosion (Alewell et al., 2015; Breshears et al., 2003).

The obtained erosion rates for LS3 and LS4 would fit better to erosion rates calculated for the Karkonosze Mts (Lower Silesia, Poland, Waroszewski et al., 2018b). The values were considerably high for the sites at relatively low elevations (Table 1). The erosion rates matched the results of Alewell et al. (2015) who investigated highly eroded soils (affected by deforestation and cattle) in the Central Swiss Alps. The loss of a major part of the loess mantle at LS3 and LS4 is most likely related to the position along the slope (summit/shoulder) and a lack of additional loess colluviation from the upslope created an imbalance between supply and material removal.

The mid- and back-slopes of LS5 and LS2, respectively, exhibited

high erosion rates. Due to the highest slope inclination at these sites ($8\text{--}12^\circ$, Table 1), these soils are considered to be particularly prone to mass transport (Sanjuán et al., 2014; Vanini and Amini, 2017). The erosion rates were generally lower than those at sites LS3 and LS4, which suggests that land use is a decisive factor. Mass wasting and runoff processes, which probably occurred during late MIS2, contributed to a high loss of the loess cover in the long-term, so that the threshold values of erosion for forest soils in Europe (Cerdan et al., 2010; Verheijen et al., 2009) were exceeded.

Site LS1 exhibited lower erosion rates ($0.11\text{--}0.78 \text{ t ha}^{-1} \text{ yr}^{-1}$ when assuming a 14 kyr soil age and $0.34\text{--}1.68 \text{ t ha}^{-1} \text{ yr}^{-1}$, when assuming a soil age of 21 kyr; Table 7). These values are closer to the lower limit of the erosion rate range calculated for Karkonosze Mts. (Waroszewski et al., 2018b) and below the tolerable erosion rates for Europe (Verheijen et al., 2009). The loess mantle at LS1 had the highest content of cosmogenic ^{10}Be ($2.33\text{--}2.31 \times 10^8$ atoms g^{-1} , Table 6). The shoulder position and low slope certainly helped preserving the soil and loess mantle. The current 78 cm thick loess mantle of LS1 (Table 2) is relatively deep compared to the other sites that have a loess cover of only 28–33 cm (Table 2).

Regardless of the site position on the slope, the erosion rates are often relatively high. Using cosmogenic in-situ ^{10}Be , Loba et al. (2021) estimated long-term erosion rates of soils on loess to 0.46 to $0.85 \text{ t ha}^{-1} \text{ yr}^{-1}$. The profiles LS3–LS5 exhibited about a double high rate. Modern clay illuviation created well-developed Bt horizons usually between 33 and 95 cm and a depletion zone that persisted even as an independent horizon (profiles LS2 and LS4). This indicates that post-pedogenic erosion was not very high. The calculated thickness of the loess mantles suggests that a few dm to about 3 m were removed. A considerable part of this loss can probably be attributed to pre-pedogenic loess erosion or a stage at which soil cover by plants was incomplete.

5.3. Stability and recovery of the loess mantles on the different basal substrates

The morphology of soils developing from loess-bearing slope deposits indicates their complexity (Fig. 2). Aeolian silt contributes to soil formation and creates starting conditions for pedogenesis (Waroszewski et al., 2018b, 2020). We hypothesised that alternating phases of loess deposition and slope erosion occurred during the Late Glacial and Early Holocene, which most likely changed the original thickness of the loess mantles.

Although pedogenesis was constantly interrupted by multiple accumulation and erosion events (reworking), Luvisols could develop (Table 1). In such thick loess mantles, it seems impossible that the soils underwent only one phase of pedogenesis. The calculated primary thickness of the loess mantles, together with the contemporary morphology of the soils, suggests that the Luvisols underwent at least two phases of pedogenesis. This assumption matches the hypothesis suggested by Waroszewski et al. (2020) on the Ślęza Massif soils (Lower Silesia) where traces of illuviation during both the Late Glacial and Early Holocene were recognised. Based on this, we suggest four main phases that shaped today's loess-mantled soils:

1) Pre-exposure to ^{10}Be accumulation: At least some of the underlying substrates hold significantly more ^{10}Be than those accumulated in the topsoil, for example LS2. However, these materials did not reveal clear features of clay translocation. Therefore, it seems that such slope sediments persisted on slopes for a long time before the Late Pleniglacial and received a substantial input of meteoric ^{10}Be .

2) Loess deposition: the pre-exposed material was covered with loess. The main loess deposition phases took place in Lower Silesia in the Upper Pleniglacial (MIS2) (Moska et al., 2011, e.g., Biały Kościół loess-paleosol sequence). The strength of loess-blowing/spreading was high enough to affect even locally isolated basins (e.g., the Kłodzko Basin, Fig. 1). We excluded soil formation during the main loess deposition episodes because of their high rates and conditions that did not

allow for a leaching of carbonates.

3) Erosion event: In a further stage, the original thick loess mantles were subjected to erosion during and after the Late Pleniglacial glacial (Fig. 3; Rea et al., 2020). At some sites, the redistribution processes seem to have been intense and contributed to a significant shallowing of the loess mantles (e.g., LS3). Waroszewski et al. (2020) provided strong evidence of such redeposition processes in a thin loess cover (dated to 14.2 ka, Oldest Dryas) hosting Alisol; therefore, the erosion events must have occurred before the starting point of pedogenesis. Based on our data it is impossible to determine the onset of the erosion or separate it into individual phases. Slope instability caused the translocation of the silty mantle to lower topographic positions and, at the same time, the supply medium for the soils located at shoulders/backslope positions (soils LS2 and LS5; Drohan et al., 2020; Fig. 3). During the Late Glacial, high morphological slope activity was possible due to the palaeoclimatic conditions with dry summers and very cold winters with deep winter soil frost that favour solifluction and slope wash processes (Veit et al. 2017).

4) Soil formation followed by modern soil erosion (Holocene): With the end of climate cooling in the Younger Dryas, environmental and ecological conditions were more favourable. According to Veit et al. (2017), near-surface processes became less intense during the Early Holocene ~ 7.5 ka, the slopes were stabilised and natural conditions minimised slope-wash processes (Fig. 3). As a result of the climatic and topographic conditions and the lack of periglacial slope processes, soil development continued (Veit et al., 2017). This phase of intensive

pedogenesis in soils from loess was also reported by Waroszewski et al. (2020) who showed micromorphological evidence from modern Bt horizons (well-developed microlaminated clay coatings) indicating the main period of Luvisol development in the area of Lower Silesia. Holocene clay eluviation and illuviation in Lower Silesia were also reported by Kabała et al. (2019).

With the advent of agriculture and in particular its mechanisation and industrialisation during the last few decades, soil erosion rates increased again dramatically giving rise to very high losses. Loba et al., (2021) reported short-term (last few decades) rates of up to 10 times (1.17 – 10.93 t ha⁻¹ yr⁻¹) higher than long-term (millenia) rates for loess areas of Central Europe.

6. Conclusions

The distribution of meteoric ¹⁰Be in the soil profiles with loess over granite or basalt slope sediments was affected by clay translocation which contributed to its accumulation in the subsoil. However, the soils developed on loess overlying Permian sandstone showed a gradually decreasing content of ¹⁰Be with depth, suggesting an earlier stage of pedogenesis with no translocation by clay particles. The decrease in ¹⁰Be with depth on glacio-fluvial sediments was favoured by the friable or very friable consistency of the soils that contributed to an easier leaching of ¹⁰Be. The noticeably high amount of ¹⁰Be in the serpentinite basal layers may derive from ¹⁰Be atmospheric input prior to the major loess

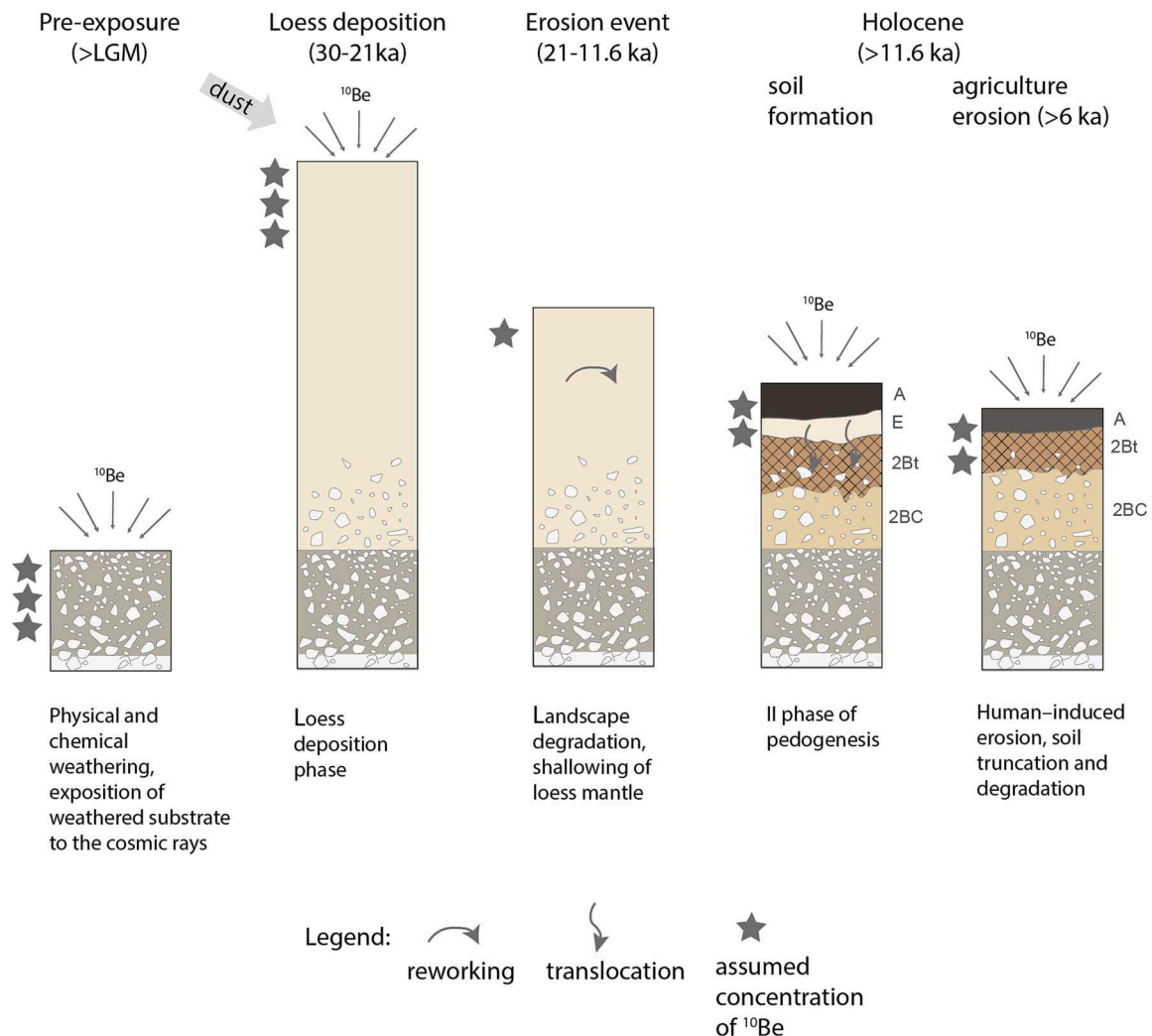


Fig. 3. Model of thin loess mantles transformation and pedogenesis in SW Poland.

deposition during the Last Glacial Maximum.

The loess mantles on granite and glacio-fluvial sediments were eroded the most, also reflected in the high reduction of their initial thickness. The erosion rates are often related to the position along the slope. Although the mid- and back-slope locations and the position with the highest inclination were considered to be more prone to erosion, the loess overlying the basal regolite and serpentinite revealed lower erosion rates. The most stable loess mantle was found on the Permian sandstone.

We used several scenarios for modelling soil erosion rates. The most reasonable erosion rates are achieved when assuming that precipitation rates in the Pleistocene were about 25% of those of the Holocene. The soil erosion and thus soil redistribution rates were comparatively high.

The evolution of loess-mantled soils encompasses several phases. Thick loess mantles developed between 30 and 21 ka (the main loess accumulation period in the region). Erosion processes occurred after loess mantle stabilisation and contributed to a considerable change in their original thickness. There is evidence of a Lateglacial clay translocation for some of the sites. The Holocene pedogenesis took place within an already thinner loess layer, which was later further shallowed due to agricultural practices.

Declaration of Competing Interest

The authors declare that they have no known competing financial interests or personal relationships that could have appeared to influence the work reported in this paper.

Data availability

Data will be made available on request.

Acknowledgements

This research was financed by the Polish National Agency for Academic Exchange (NAWA Poland) Project No. PPN/IWA/2019/1/00078/U/00001 and Wrocław University of Environmental and Life Sciences (Poland) as part of the Ph.D. research program Innovative Scientist No N060/0004/22 (both awarded to Joanna Beata Kowalska), as well as by the National Science Center (Poland) project Opus 16 no. 2018/29/B/ST10/01282 (awarded to Jarosław Waroszewski). This study was also supported by the Foundation for Polish Science (FNP). The authors would like to thank Dr. Tobias Sprafke for his kind suggestions, which helped to improve the manuscript. We also thank three anonymous reviewers for their contribution to an earlier version of the paper. The APC/BPC is financed by Wrocław University of Environmental and Life Sciences.

References

- Aldahan, A., Ye, H., Possnert, G., 1999. Distribution of beryllium between solution and minerals (biotite and albite) under atmospheric conditions and variable pH. *Chem. Geol.* 156 (1–4), 209–229.
- Alewell, C., Egli, M., Meusburger, K., 2015. An attempt to estimate tolerable soil erosion rates by matching soil formation with denudation in Alpine grasslands 1383–1399. [10.1007/s11368-014-0920-6](https://doi.org/10.1007/s11368-014-0920-6).
- Arata, L., Meusburger, K., Frenkel, E., A'Campo-Neuen, A., Iurian, A.R., Ketterer, M.E., Mabit, L., Alewell, C., 2016a. Modelling deposition and erosion rates with radionuclides (MODERN) - Part 1: a new conversion model to derive soil redistribution rates from inventories of fallout radionuclides. *J. Environ. Radioact.* 162–163, 45–55. <https://doi.org/10.1016/j.jenvrad.2016.05.008>.
- Arata, L., Alewell, C., Frenkel, E., A'Campo-Neuen, A., Iurian, A.R., Ketterer, M.E., Mabit, L., Meusburger, K., 2016b. Modelling deposition and erosion rates with radionuclides (MODERN) - Part 2: a comparison of different models to convert $^{239+240}\text{Pu}$ inventories into soil redistribution rates at unploughed sites. *J. Environ. Radioact.* 162–163, 97–106. <https://doi.org/10.1016/j.jenvrad.2016.05.009>.
- Awdankiewicz, M., Kurowski, L., Mastalerz, K., Raczynski, P., 2003. The intra sudetic basin: record of sedimentary and volcanic processes in late- to post-orogenic setting. *Geolines* 16, 165–183.
- Bac-Bronowicz, J., Grzempowski, P., 2018. Regionalization of geographical space according to selected topographic factors in reference to spatial distribution of precipitation: application of artificial neural networks in GIS. *Environ. Earth Sci.* 77, 631. <https://doi.org/10.1007/s12665-018-7811-x>.
- Baykal, Y., Stevens, T., Engström-Johansson, A., Skurzynski, J., Zhang, H., He, J., Lu, H., Adamiec, G., Köllinger, C., Jary, Z., 2021. Detrital zircon U-Pb age analysis of last glacial loess sources and proglacial sediment dynamics in the Northern European Plain. *Quat. Sci. Rev.* 274, 107265. <https://doi.org/10.1016/j.quascirev.2021.107265>.
- Boschi, V., Willenbring, J.K., 2021. Chemical and physical drivers of beryllium retention in two soil endmembers. *Sci. Total Environ.* 754, 141591. <https://doi.org/10.1016/j.scitotenv.2020.141591>.
- Breshears, D.D., Whicker, J.J., Johansen, M.P., Pinder, J.E., 2003. Wind and water erosion and transport in semi-arid shrubland, grassland and forest ecosystems: quantifying dominance of horizontal wind-driven transport. *Earth Surface Process. Landforms* 28 (11), 1189–1209.
- Calitri, F., Sommer, M., Norton, K., Temme, A., Brandová, D., Portes, R., Christl, M., Ketterer, M.E., Egli, M., 2019. Tracing the temporal evolution of soil redistribution rates in an agricultural landscape using $^{239+240}\text{Pu}$ and ^{10}Be . *Earth Surf. Process. Landforms* 44, 1783–1798. <https://doi.org/10.1002/esp.4612>.
- Cerdan, O., Govers, G., Le Bissonnais, Y., Van Oost, K., Poesen, J., Saby, N., Gobin, A., Vacca, A., Quinton, J., Auerswald, K., Klik, A., Kwaad, F.J.P.M., Raclot, D., Ionita, I., Rejman, J., Rousseva, S., Muxart, T., Roxo, M.J., Dostal, T., 2010. Rates and spatial variations of soil erosion in Europe: a study based on erosion plot data. *Geomorphology* 122, 167–177. <https://doi.org/10.1016/j.geomorph.2010.06.011>.
- Chen, P., Yi, P., Czymzik, M., Aldahan, A., Ljung, K., Yu, Z., Hou, X., Zheng, M., Chen, X., Possnert, G., 2020. Relationship between precipitation and ^{10}Be and impacts on soil dynamics. *Catena* 195, 104748. <https://doi.org/10.1016/j.catena.2020.104748>.
- Christl, M., Vockenhuber, C., Kubik, P.W., Wacker, L., Lachner, J., Alfimov, V., Snyal, H. A., 2013. The ETH Zurich AMS facilities: performance parameters and reference materials. *Nucl. Instrum. Methods Phys. Res. Sect. B* 294, 29–38. <https://doi.org/10.1016/j.nimb.2012.03.004>.
- Costantini, E.A.C., Carnicelli, S., Sauer, D., Priori, S., Andreetta, A., Kadereit, A., Lorenzetti, R., 2018. Loess in Italy: genesis, characteristics and occurrence. *Catena* 168, 14–33. <https://doi.org/10.1016/j.catena.2018.02.002>.
- Delijska, A., Blazheva, T., Petkova, L., Dimov, L., 1988. Fusion with lithium borate as sample preparation for ICP and AAS analysis. *Fresenius' Z. Anal. Chem.* 332, 362–365. <https://doi.org/10.1007/BF00468816>.
- Döhler, S., Terhorst, B., Frechen, M., Zhang, J., Damm, B., 2018. Chronostratigraphic interpretation of intermediate layer formation cycles based on OSL-dates from intercalated slope wash sediments. *Catena* 162, 278–290.
- Drohan, P.J., Raab, T., Hirsch, F., 2020. Distribution of silty mantles in soils of the Northcentral Appalachians, USA. *Catena* 194, 104701. <https://doi.org/10.1016/j.catena.2020.104701>.
- Drozd, J., Jamroz, E., Licznar, M., Weber, J., 1994. Relationships between different elements of the soil fertility and their effect on the horse bean yield. *Nove poznatki Zvysoania Produkcyjnej Schopnosti Pod, VSP Nitra*, pp. 16–21.
- Drozd, J., Piatek, J., Labaz, B., 2007. Properties of the Chernozem soils in Kłodzko basin. *Zesz. Probl. Postep. Nauk. Rol.* 520, 447–454.
- Dubinska, E., Nejbort, K., Bylina, P., 2010. Olivines from ultramafic rocks of Jordanów-gogołów serpentinite massif (Sudetic ophiolite) – A complex interplay of petrogenetic processes. *Przegląd Geol.* 58, 506–515.
- Egli, M., Brandová, D., Böhlert, R., Favilli, F., Kubik, P., 2010. ^{10}Be inventories in Alpine soils and their potential for dating land surfaces. *Geomorphology* 119, 62–73. <https://doi.org/10.1016/j.geomorph.2010.02.019>.
- FAO, 2006. *Guidelines for Soil Description*, 4th edn. FAO, Rome.
- Frechen, M., Oches, E.A., Kohfeld, K.E., 2003. Loess in Europe e mass accumulation rates during the Last Glacial Period. *Quat. Sci. Rev.* 22.
- Gallet, S., Jahn, B., Van Vliet-Lanoë, B., Dia, A., Rosello, E., 1998. Loess geochemistry and its implications for particle origin and composition of the upper continental crust. *Earth Planet. Sci. Lett.* 156, 157–172.
- Gil, G., Barnes, J.D., Boschi, C., Gunia, P., Szakmány, G., Bendő, Z., Raczynski, P., Péterdi, B., 2015. Origin of serpentinite-related nephrite from Jordánów and adjacent areas (SW Poland) and its comparison with selected nephrite occurrences. *Geol. Q.* 59, 457–472. <https://doi.org/10.7306/gq.1228>.
- Graly, J.A., Reusser, L.J., Bierman, P.R., 2011. Short and long-term delivery rates of meteoric ^{10}Be to terrestrial soils. *Earth Planet. Sci. Lett.* 302, 329–336. <https://doi.org/10.1016/j.epsl.2010.12.020>.
- Gu, Z.Y., Lal, D., Liu, T.S., Southon, J., Caffee, M.W., Guo, Z.T., Chen, M.Y., 1996. Five million year ^{10}Be record in Chinese loess and red-clay: climate and weathering relationships. *Earth Planet. Sci. Lett.* 144 (1e2), 273–287.
- Haase, D., Fink, J., Haase, G., Ruske, P., Pesci, M., Richter, H., Altermann, M., Jager, K. D., 2007. Loess in Europe—Its spatial distribution based on a European Loess Map, scale 1:2,500,000. *Quat. Sci. Rev.* 26 (9), 1301–1312. <https://doi.org/10.1016/j.quascirev.2007.02.003>.
- Heikkilä, U., Beer, J., Feichter, J., 2008. Modeling cosmogenic radionuclides ^{10}Be and ^{7}Be during the Maunder Minimum using the ECHAM5-HAM general circulation model. *Atmos. Chem. Phys.* 8, 2797–2809.
- Heyman, B.M., Heyman, J., Fickert, T., Harbor, J.M., 2013. Paleo-climate of the central European uplands during the last glacial maximum based on glacier mass-balance modelling. *Quat. Res.* 79, 49–54. <https://doi.org/10.1016/j.yqres.2012.09.005>.
- Hidy, A.J., Gosse, J.C., Sanborn, P., Froese, D.G., 2018. Age-erosion constraints on an Early Pleistocene paleosol in Yukon, Canada, with profiles of ^{10}Be and ^{26}Al : evidence for a significant loess cover effect on cosmogenic nuclide production rates. *Catena* 165, 260–271. <https://doi.org/10.1016/j.catena.2018.02.009>.
- IUSS Working Group WRB, 2022. *World Reference Base for Soil Resources. International soil classification system for naming soils and creating legends for maps*, 4th edition. FAO, Rome, Vienna, Austria.

- Jacobs, P.M., Mason, J.A., Hanson, P.R., 2012. Loess mantle spatial variability and soil horizonation, southern Wisconsin, USA. *Quat. Int.* 265, 43–53. <https://doi.org/10.1016/j.quaint.2012.01.017>.
- Jagercikova, M., Cornu, S., Bourlés, D., Antoine, P., Mayor, M., Guillou, V., 2015. Understanding long-term soil processes using meteoric ^{10}Be : A first attempt on loessic deposits. *Quat. Geochronol.* 27, 11–21. <https://doi.org/10.1016/j.quageo.2014.12.003>.
- Jary, Z., 1999. Ostatni cykl lesowy w Polsce SW. In: Jary, Z. (Ed.), III Seminarium Lessowe– Geneza i wiek pokrywowych utworów pylastych południowo-zachodniej Polski. Uniwersytet Wrocławski, Wrocław-Bożków, Poland, pp. 35–37.
- Jary, Z., 2010. Loess–soil sequences as a source of climatic proxies: an example from SW Poland. *Geologija* 52, 40–45.
- Jary, Z., Kida, J., 2000. Loess particles sources, transport and deposition on the example of SW Poland. *Acta Univ. Wratislaviensis, Studia Geograficzne LXXIV*, pp. 71–77.
- Kabala, C., Bekier, J., Bińczycki, T., Bogacz, A., Bojko, O., Cuske, M., Cwięlag-Piasecka, I., et al., 2015a. Soils of Lower Silesia: Origins. Diversity and Protection, PTG, PTSH, Wrocław.
- Kabala, C., Bekier, J., Bińczycki, T., Bogacz, A., Bojko, O., Cuske, M., Cwięlag-Piasecka, I., Dębicka, M., Gałka, B., Gersztyn, L., Głina, B., Jamroz, E., Jezierski, P., Karczewska, A., Kaszubkiewicz, J., Kawalko, D., Kierczak, J., Kocowicz, A., Krupski, M., Kusza, G., Łabaz, B., Marzec, M., Medyńska-Juraszek, A., Musztyfaga, E., Perlak, Z., Pędziwiatr, A., Pora, E., Przybył, A., Strączyńska, S., Szopka, K., Tyska, R., Waroszewski, J., Weber, J., Woźniczka, P., 2015. Soils of Lower Silesia: Origins, Diversity and Protection. PTG, PTSH, Wrocław (256 pp.).
- Kabala, C., Musztyfaga, E., 2016. Clay-illuvial soils in the Polish and international soil classifications. *Soil Sci. Annu.* 66, 204–213.
- Kabala, C., Przybył, A., Krupski, M., Łabaz, B., Waroszewski, J., 2019. Origin, age and transformation of Chernozems in northern Central Europe – New data from Neolithic earthen barrows in SW Poland. *Catena* 180, 83–102. <https://doi.org/10.1016/j.catena.2019.04.014>.
- Kierczak, J., Pędziwiatr, A., Waroszewski, J., Modelska, M., 2016. Mobility of Ni, Cr and Co in serpentine soils derived on various ultrabasic bedrocks under temperate climate. *Geoderma* 268, 78–91.
- Kleber, A., Terhorst, B., 2013. Mid-latitude slope deposits (Cover Beds) (Developments in Sedimentology Vol. 66. Elsevier, Amsterdam.
- Kowalska, J.B., Vöggtli, M., Kierczak, J., Egli, M., Waroszewski, J., 2022. Clay mineralogy fingerprinting of loess-mantled soils on different underlying substrates in the south-western Poland. *Catena* 210. <https://doi.org/10.1016/j.catena.2021.105874>.
- Kryza, R., Pin, C., 2010. The Central-Sudetic ophiolites (SW Poland): Petrogenetic issues, geochronology and palaeotectonic implications. *Gondwana Res.* 17, 292–305.
- Łabaz, B., Kabala, C., 2014. Origin, properties and classification of “black earths” in Poland. *Soil Sci. Annu.* 65, 80–90.
- Łabaz, B., Musztyfaga, E., Waroszewski, J., Bogacz, A., Jezierski, P., Kabala, C., 2018. Landscape-related transformation and differentiation of Chernozems – catenary approach in the Silesian Lowland. SW Poland. *Catena* 161. <https://doi.org/10.1016/j.catena.2017.10.003>.
- Łabaz, B., Kabala, C., Waroszewski, J., 2019. Ambient geochemical baselines for trace elements in Chernozems—approximation of geochemical soil transformation in an agricultural area. *Environ. Monit. Assess.* 191, 19.
- Lal, D., 2001. New Nuclear Methods for Studies of Soil Dynamics Utilizing Cosmic Ray Produced Radionuclides. Stott, D.E., Mohtar, R.H., Steinhardt, G.C. (Eds.) Sustain. Glob. Farm. 10th Int. Soil Conserv. Organ. Meet. Purdue Univ. USDA-ARS Natl. Soil Eros. Res. Lab. 1044–1052.
- Lehmkuhl, F., Nett, J.J., Pötter, S., Schulte, P., Sprafke, T., Jary, Z., Antoine, P., Wacha, L., Wolf, D., Zerboni, A., Hošek, J., Marković, S.B., Obrecht, I., Sümegi, P., Veres, D., Zeeden, C., Boemke, B., Schaubert, V., Viehweger, J., Hambach, U., 2021. Loess landscapes of Europe – Mapping, geomorphology, and zonal differentiation. *Earth-Sci. Rev.* 215. <https://doi.org/10.1016/j.earscirev.2020.103496>.
- Licznar, M., 1976. Properties and genesis of some chernozems in the Glubczyce Plateau. *Roczniki Gleboznawcze. Soil Sci. Annu.* 27 (4), 107–148.
- Loba, A., Waroszewski, J., Tikhomirov, D., Calitri, F., Christl, M., Sykula, M., Egli, M., 2021. Tracing erosion rates in loess landscape of the Trzebnica Hills (Poland) over time using fallout and cosmogenic nuclides. *J. Soils Sediments* 21, 2952–2968. <https://doi.org/10.1007/s11368-021-02996-x>.
- Lorz, C., Frühauf, M., Mailänder, R., Phillips, J.D., Kleber, A., 2013. Influence of cover beds on soils. In: Kleber, A., Terhorst, B. (Eds.), Mid-Latitude Slope Deposits (Cover-Beds). Developments in Sedimentology. 66. pp. 95–125.
- Luehmann, M.D., Schaezel, R.J., Miller, B.A., Bigsby, M.E., 2013. Thin, Pedoturbated, And locally sourced loess in the western Upper Peninsula of Michigan. *Aeolian Res.* 8, 85–100. <https://doi.org/10.1016/j.aeolia.2012.11.003>.
- Maejima, Y., Matsuzaki, H., Higashi, T., 2005. Application of cosmogenic ^{10}Be to dating soils on the raised coral reef terraces of Kikai Island, southwest Japan. *Geoderma* 126, 389–399.
- Malkiewicz, M., Waroszewski, J., Bojko, O., Egli, M., Kabala, C., 2016. Holocene vegetation history and soil development reflected in the lake sediments of the Karkonosze Mountains (Poland). *The Holocene* 26, 890–905.
- Marks, L., 2005. Pleistocene glacial limits in the territory of Poland. *Prz. Geol.* 53, 988–993.
- Marquard, J., Aalto, R.E., Barrows, T.T., Fisher, B.A., Aufdenkampe, A.K., Stone, J.O., 2019. Topographic variation in soil erosion and accumulation determined with meteoric ^{10}Be . *Be* 111, 98–111. <https://doi.org/10.1002/esp.4483>.
- Marshall, J.A., Roering, J.J., Gavin, D.G., Granger, D.E., 2017. Late Quaternary climatic controls on erosion rates and geomorphic processes in western Oregon, USA. *Geol. Soc. Am. Bull.* 129, 715–731. <https://doi.org/10.1130/B31509.1>.
- Maxeiner, S., Snyal, H.A., Christl, M., Suter, M., Müller, A., Vockenhuber, C., 2019. Proof-of-principle of a compact 300 kV multi-isotope AMS facility. *Nucl. Instrum. Methods Phys. Res. Sect. B* 439, 84–89. <https://doi.org/10.1016/j.nimb.2018.11.028>.
- Migoń, P., Jancewicz, K., Kasprzak, M., 2020. Inherited periglacial geomorphology of a basalt hill in the Sudetes, Central Europe: Insights from LiDAR-aided landform mapping. *Permafrost. Periglac. Process.* 31, 587–597. <https://doi.org/10.1002/ppp.2062>.
- Moska, P., Adamiec, G., Jary, Z., 2011. OSL dating and lithological characteristics of loess deposits from biały kocioł. *Geochronometria* 38, 162–171. <https://doi.org/10.2478/s13386-011-0013-x>.
- Moska, P., Jary, Z., Adamiec, G., Bluszcz, A., 2019. Chronostratigraphy of a loess-palaeosol sequence in Biały Kocioł Poland using OSL and radiocarbon dating. *Quat. Int.* 502, 4–17. <https://doi.org/10.1016/j.quaint.2018.05.024>.
- Norton, K.P., von Blanckenburg, F., Kubik, P.W., 2010. Cosmogenic nuclide derived rates of diffusive and episodic erosion in the glacially sculpted upper Rhone Valley, Swiss Alps. *Earth Surf. Process. Landforms* 35, 651–662. <https://doi.org/10.1002/esp.1961>.
- Pawlak, W., 2008. Atlas of Lower and Opole Silesia, 2nd ed. Wrocław University, Wrocław, Poland.
- Pędziwiatr, A., Kierczak, J., Waroszewski, J., Ratié, G., Quantin, C., Ponzever, E., 2018. Rock-type control of Ni, Cr, and Co phytoavailability in ultramafic soils. *Plant Soil* 423, 339–362.
- Puchol, N., Lavé, J.O., Lupker, M., Blard, P.H., Gallo, F., France-Lanord, C., 2014. Grain-size dependent concentration of cosmogenic ^{10}Be and erosion dynamics in a landslide-dominated Himalayan watershed. *Geomorphology* 224, 55–68. <https://doi.org/10.1016/j.geomorph.2014.06.019>.
- Rea, B.R., Pellitero, R., Spagnolo, M., Hughes, P., Ivy-Ochs, S., Renssen, H., Ribolini, A., Bakke, J., Lukas, S., Braithwaite, R.J., 2020. Atmospheric circulation over Europe during the Younger Dryas. *Sci. Adv.* 6, 1–14. <https://doi.org/10.1126/sciadv.aba4844>.
- Ritchie, J.C., Ritchie, C.A., 2007. Bibliography of publications of $^{137}\text{Cesium}$ studies related to erosion and sediment deposition. USDA-ARS Hydrology and Remote Sensing Laboratory, United States Department of Agriculture, Agricultural Research Service.
- Rousseau, D.D., Derbyshire, E., Antoine, P., Hatte, 2007. Loess records – Europe. In: Elias, S. (Ed.), *The Encyclopedia of Quaternary Sciences*. Elsevier, Amsterdam, pp. 1440–1456.
- Sanjuán, Y., Gómez-Villar, A., Nadal-Romero, E., Álvarez-Martínez, J., Arnáez, J., Serrano-Muela, M.P., Rubiales, J.M., González-Sampériz, P., García-Ruiz, J.M., 2014. Linking land cover changes in the subalpine and montane belts to changes in a torrential river. *Land Degrad. Dev.* <https://doi.org/10.1002/ldr.2294>.
- Schaezel, R., Bettis, E., Crouvi, O., Fitzsimmons, K., Grimley, D., Hambach, U., Zech, R., 2018. Approaches and challenges to the study of loess—Introduction to the LoessFest Special Issue. *Quaternary Res.* 89 (3), 563–618. [10.1017/qua.2018.15](https://doi.org/10.1017/qua.2018.15).
- Schaffernicht, E.J., Ludwig, P., Shao, Y., 2020. Linkage between dust cycle and loess of the Last Glacial Maximum in Europe. *Atmos. Chem. Phys.* 20, 4969–4986. <https://doi.org/10.5194/acp-20-4969-2020>.
- Scheib, A. J., Birke, M., Dinelli, E., GEMAS Project Team., 2014. Geochemical evidence of aeolian deposits in European soils. *Boreas* Vol. 43, pp. 175–192.
- Shen, C., Beer, J., Kubik, P.W., Suter, M., Borkovec, M., Liu, T.S., 2004. Grain size distribution, ^{10}Be content and magnetic susceptibility of micrometer-nanometer loess materials. *Nucl. Instrum. Methods Phys. Res. Sect. B Beam Interact. Mater. Atoms* 223–224, 613–617.
- Sprafke, T., 2016. *Loss in Niederösterreich - Archiv quartärer Klima- und Landschaftsveränderungen*. Würzburg University Press, Würzburg, p. 272.
- Valde-Nowak, P., Lanczont, M., 2021. State-of-the-art overview of the Loess Palaeolithic of Poland. *J. Quat. Sci.* 36, 1341–1352. <https://doi.org/10.1002/jqs.3356>.
- Van Reeuwijk, L.P., 2002. *Procedures for Soil Analysis*, 6th edn. ISRIC, Wageningen.
- Vanini, H.S., Amini, M., 2017. Assessment of soil erosion on hillslopes (A case study carried out in the Ashan Drainage Basin, Iran). *Eur. J. Environ. Sci.* 7, 99–107. [10.14712/23361964.2017.8](https://doi.org/10.14712/23361964.2017.8).
- Veit, H., Trauerstein, M., Preusser, F., Messmer, T., Gnägi, C., Zech, R., Wüthrich, L., 2017. Late glacial/early holocene slope deposits on the swiss plateau: genesis and palaeo-environment. *Catena* 158, 102–112. <https://doi.org/10.1016/j.catena.2017.06.012>.
- Verheijen, F.G.A., Jones, R.J.A., Rickson, R.J., Smith, C.J., 2009. Earth-science reviews tolerable versus actual soil erosion rates in Europe. *Earth Sci. Rev.* 94, 23–38. <https://doi.org/10.1016/j.earscirev.2009.02.003>.
- Vonmoos, M., Beer, J., Muscheler, R., 2006. Large variations in Holocene solar activity: constraints from ^{10}Be in the Greenland Ice Core Project ice core. *J. Geophys. Res.* 111, A10105.
- Wallbrink, P., Murray, A., 1994. Fallout of ^{7}Be in south eastern Australia. *J. Environ. Radioact.* 25 (3), 213–228.
- Waroszewski, J., Sprafke, T., Kabala, C., Musztyfaga, E., Łabaz, B., Woźniczka, P., 2018a. Aeolian silt contribution to soils on mountain slopes (Mt. Słęża, southwest Poland). *Quat. Res. (United States)* 89, 702–717. <https://doi.org/10.1017/jqs.2017.76>.
- Waroszewski, J., Egli, M., Brandová, D., Christl, M., Kabala, C., Malkiewicz, M., Kierczak, J., Głina, B., Jezierski, P., 2018b. Identifying slope processes over time and their imprint in soils of medium-high mountains of Central Europe (the Karkonosze Mountains, Poland). *Earth Surf. Process. Landforms* 4305. <https://doi.org/10.1002/esp.4305>.
- Waroszewski, J., Sprafke, T., Kabala, C., Kobierski, M., Kierczak, J., Musztyfaga, E., Loba, A., Mazurek, R., Łabaz, B., 2019. Tracking textural, mineralogical and geochemical signatures in soils developed from basalt-derived materials covered with loess sediments (SW Poland). *Geoderma* 337, 983–997. <https://doi.org/10.1016/j.geoderma.2018.11.008>.

- Waroszewski, J., Sprafke, T., Kabala, C., Musztyfaga, E., Kot, A., Tsukamoto, S., Frechen, M., 2020. Chronostratigraphy of silt-dominated Pleistocene periglacial slope deposits on Mt. Słęża (SW, Poland): Palaeoenvironmental and pedogenic significance. *Catena* 190, 104549. <https://doi.org/10.1016/j.catena.2020.104549>.
- Waroszewski, J., Pietranik, A., Sprafke, T., Kabala, C., Frechen, M., Jary, Z., Kot, A., Tsukamoto, S., Meyer-Heintze, S., Krawczyk, M., Łabaz, B., Schultz, B., Erban Kochergina, Y.V., 2021. Provenance and paleoenvironmental context of the Late Pleistocene thin aeolian silt mantles in south-west Poland – a widespread parent material for soils. *Catena* 204. <https://doi.org/10.1016/j.catena.2021.105377>.
- Weber, J., 1982. Genesis and properties of soils derived from serpentinites in Lower Silesia. Part IV. Characteristics of colloidal fraction. *Roczniki Gleboznawcze (in Polish)* 33, 2, 73–84.
- Willenbring, J.K., von Blanckenburg, F., 2010. Meteoric cosmogenic Beryllium-10 adsorbed to river sediment and soil: Applications for Earth-surface dynamics. *Earth-Sci. Rev.* 98, 105–122. <https://doi.org/10.1016/j.earscirev.2009.10.008>.
- Williams, M., 2015. Interactions between fluvial and eolian geomorphic systems and processes: examples from the Sahara and Australia. *Catena* 134, 4–13.
- Wittmann, H., von Blanckenburg, F., Dannhaus, N., Bouchez, J., Gaillardet, J., Guyot, J., Maurice, L., Roig, H., Filizola, N., Christl, M., 2015. A test of the cosmogenic ^{10}Be (meteoric)/ ^9Be proxy for simultaneously determining basin-wide erosion rates, denudation rates, and the degree of weathering in the Amazon basin. – *J. Geophys. Res.* 120 (12), 2498–2528. <https://doi.org/10.1002/2015JF003581>.
- Wojciechowska, I., 1966. Budowa geologiczna metamorfiku dorzecza Ścinaki Kłodzkiej. *Geol. Sudetica* 2, 261–296.
- Wyshnytzky, C., Ouimet, W.B., McCarthy, J., Dethier, D.P., Shroba, R.R., Bierman, P.R., Rood, D.H., 2015. Meteoric ^{10}Be , clay, and extractable iron depth profiles in the Colorado Front Range: implications for understanding soil mixing and erosion. *Catena* 127, 32–45.
- Yang, F., Karius, V., Sauer, D., 2020. Quantification of loess proportions in Pleistocene periglacial slope deposits and Holocene colluvium using grain-size data by laser diffractometry. *J. Plant Nutr. Soil Sci.* 183, 277–281.
- Yates, K., Fenton, C.H., Bell, D.H., 2018. A review of the geotechnical characteristics of loess and loess-derived soils from Canterbury, South Island, New Zealand. *Eng. Geol.* 236, 11–21.
- Zollinger, B., Alewell, C., Kneisel, C., Brandová, D., Petrillo, M., Plötze, M., Christl, M., Egli, M., 2017. Soil formation and weathering in a permafrost environment of the Swiss Alps: a multi-parameter and nonsteady-state approach. *Earth Surface Process. Landforms* 42, 814–835.